



## Crustal structure beneath China from receiver function analysis

Youlin Chen,<sup>1</sup> Fenglin Niu,<sup>2</sup> Ruifeng Liu,<sup>3</sup> Zhibin Huang,<sup>3</sup> Hrvoje Tkalčić,<sup>4</sup>  
Li Sun,<sup>3</sup> and Winston Chan<sup>1</sup>

Received 13 February 2009; revised 1 September 2009; accepted 30 September 2009; published 13 March 2010.

[1] We collected and processed a large amount of high-quality broadband teleseismic waveform data recorded by the 48 Chinese National Digital Seismic Network stations to estimate large-scale lateral variations of crustal thickness and  $V_p/V_s$  ratio (hence Poisson's ratio) beneath China. A statistical method was used to select mutually coherent receiver functions at each station, which yielded over 200 traces for most of the stations. With the conventional  $H-\kappa$  (the crustal thickness and  $V_p/V_s$  ratio) approach, there is a large trade-off between  $H$  and  $\kappa$ . Consequently, multiple maxima are frequently observed in the  $H-\kappa$  domain. We introduced a weight function that measures the coherence between the  $P$ -to- $S$  conversion and the reverberation phases at each  $H-\kappa$  grid to reduce the trade-off. A 4th-root stacking method was further applied to reduce uncorrelated noise relative to the linear stack. These modifications turned out to be very effective in reducing the  $H-\kappa$  trade-off and yielded reliable estimates of crustal thickness and  $V_p/V_s$  ratio. The crust beneath eastern China is as thin as 31–33 km and the underlying Moho is relatively flat and sharp. In the western part of China, the crust is considerably thicker and shows large variations. The Moho is observed at about 51 km depth along the Tian Shan fold system and about 84 km deep beneath the central part of the Tibetan Plateau. The transition occurs at the so-called N-S belt between about 100° and 110°E, which is featured by unusually high seismicity and large gravity anomalies. The average  $V_p/V_s$  ratio over the mainland China crust is about 1.730 ( $\sigma = 0.249$ ), significantly lower than the global average 1.78 ( $\sigma = 0.27$ ) of the continental crust. This lower  $V_p/V_s$  ratio may suggest a general absence of mafic lowermost crustal layer beneath China.

**Citation:** Chen, Y., F. Niu, R. Liu, Z. Huang, H. Tkalčić, L. Sun, and W. Chan (2010), Crustal structure beneath China from receiver function analysis, *J. Geophys. Res.*, 115, B03307, doi:10.1029/2009JB006386.

### 1. Introduction

#### 1.1. Tectonics Background

[2] The geology of China has been found to be highly diverse, consisting of various tectonic zones from the ancient Archean Sino-Korean and Yangtze cratons to the young and active Tibetan Plateau formed by the Cenozoic India-Eurasia collision. China is also a country with high levels of seismic activity, and has a history of strong earthquakes that caused great loss in both life and property. Therefore, knowledge of crustal structure of China has great importance in understanding the evolution of the crust, as well as locating earthquake hypocenters and investigating the mechanism of strong earthquakes in China.

[3] The mainland of China mainly consists of nuclei of Precambrian cratons and a mosaic of later accreted microcontinents and fold belts. There are three major Precambrian

cratons: The Sino-Korea craton (also known as North China Block (NCB)), the Tarim craton, and the Yangtze craton (Figure 1). The combination of the Yangtze craton and the Cathaysia block, which consists of the south China fold belt and an underwater section to the east, constitutes the South China Block (SCB). The modern Chinese tectonics is the result of a very long and complicated evolution history of collision, underthrust, and suture between different tectonic blocks. The Permian-Triassic NCB-SCB collision and the Cenozoic India-Eurasia collision are two most significant tectonic events in shaping the landscape of China. The collision between NCB and SCB occurred as a northward underthrusting of the SCB under the NCB, and very likely it led to the uplift of the north of the suture zone along the Sulu and Qinling-Dabie orogens and the flexural subsidence of the southern zones [Vermeesch, 2003]. Almost immediately following the NCB-SCB collision, the Qiangtang block was underthrust by the amalgamated South China and Qaidam-Tarim blocks along the Jinsha suture in the northeast, and was further underthrust by the Gondwana-derived Lhasa block from the south in Cretaceous [Yin and Nie, 1996; Yin and Harrison, 2000]. At approximately 45 Ma, the India plate started to collide with Asia plate along the Indus-Tsangpo suture. The India-Eurasia collision caused the formation of the Himalayas, thickening of the Tibetan crust,

<sup>1</sup>Array Information Technology, Greenbelt, Maryland, USA.

<sup>2</sup>Department of Earth Science, Rice University, Houston, Texas, USA.

<sup>3</sup>Chinese Earthquake Network Center, China Earthquake Administration, Beijing, China.

<sup>4</sup>Research School of Earth Sciences, Australian National University, Canberra, ACT, Australia.

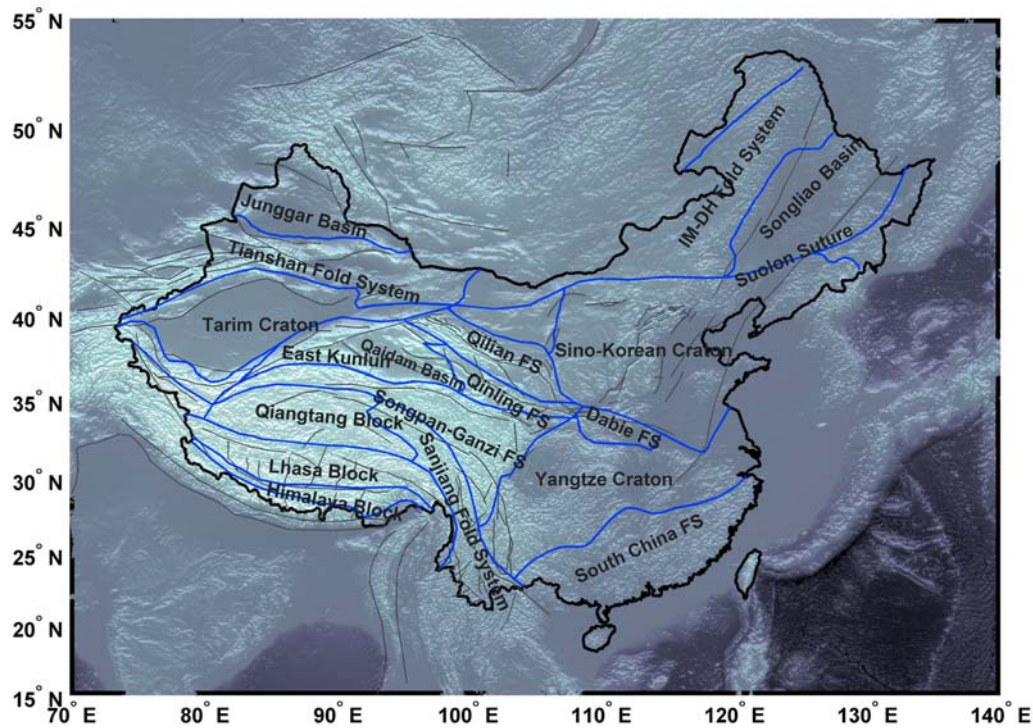


**Figure 1.** Tectonic map showing the major crustal blocks of China [see *Huang et al.*, 1980].

and uplift of the Tibetan Plateau. At the same time, the collision reactivated and deformed many of the tectonic zones such as the Tian Shan, the Altai, and the Altun Shan. Overall, this collision has led to the development of a significant contrast in crustal structure between western and eastern China. The relatively young and tectonically active western China has the thickest crust in the globe while the old and stable cratons in the eastern part of China are featured by a relatively thin to normal crust. From east to west, the crust thickens through a so-called N-S-trending belt transitional zone (approximately from 100°E to 110°E) associated with a large number of shallow focus earthquakes.

## 1.2. Geologic Implications of Crustal Thickness and $V_p/V_s$ Ratio

[4] In this study we applied the receiver function technique to estimate two parameters that describe the crust: The crustal thickness that is defined by the Moho depth, and the average crustal  $V_p/V_s$  ratio. The  $V_p/V_s$  ratio is uniquely related to the better known crustal elastic property Poisson's ratio defined by

$$\sigma = \frac{\left(\frac{V_p}{V_s}\right)^2 - 2}{2\left[\left(\frac{V_p}{V_s}\right)^2 - 1\right]} \quad (1)$$

[5] It has been generally accepted that the continental growth evolved through the amalgamation of island arcs and microcontinental blocks onto preexisting continents, and pervasive intrusion and underplating of magmas derived

from the upper mantle [Rudnick, 1995]. The thickness and composition of the crust provide tight constraints in modeling the origin and evolution of continental crust. The crustal composition is closely related to the  $V_p/V_s$  ratio, or equivalently, the Poisson's ratio,  $\sigma$ . Laboratory measurements suggest that pressure or temperature has little effect on the  $V_p/V_s$  ratio. However, the mineralogy of rocks plays a key role in the variation of  $V_p/V_s$  ratio [Christensen, 1996]. The relative abundance of quartz ( $V_p/V_s = 1.49$ ) and plagioclase ( $V_p/V_s = 1.87$ ) has a dominant effect on the  $V_p/V_s$  ratio of common igneous rocks or their metamorphosed equivalents. An increase of plagioclase content or a decrease of quartz content can increase the  $V_p/V_s$  ratio of a rock. For example, the  $V_p/V_s$  ratio increases from 1.71 for granitic rock, to 1.78 for diorite, and to 1.87 for gabbro [Tarkov and Vavakin, 1982]. The mafic/ultramafic igneous rocks usually have high  $V_p/V_s$  ratios because they usually contain gabbro and peridotite or dunite which originated from magmatic differentiation. Moreover, partial melt also has an important effect on the  $V_p/V_s$  ratio, which significantly increases with an increasing fluid fraction [Watanabe, 1993].

[6] There is no simple relationship among the crustal thickness,  $V_p/V_s$  ratio, and crustal age. On the basis of 76 worldwide samples, Zandt and Ammon [1995] suggested that the  $V_p/V_s$  ratio roughly increases with the age of the crust. On the other hand, Durrheim and Mooney [1994] compared crustal models from many parts of the world and found that Proterozoic terranes, in general, have a thicker crust than the Archean. They further concluded that the difference is due to the existence or lack of a several-kilometer-thick lowermost mafic layer. The conclusion on the relationship between age and  $V_p/V_s$  ratio is highly controversial since the later measurements from many parts

of the world appear to be much more complicated. For example, studies from southern African crust [Niu and James, 2002; Nair et al., 2006] found that the eastern Zimbabwe and the southern Kaapvaal cratons are characterized by a thin crust (about 38 km) with a low  $V_p/V_s$  ratio (about 1.73). Chevrot and van der Hilst [2000] argued for substantial variations in the  $V_p/V_s$  ratio in different tectonic units of Australian crust. For the Proterozoic crust, they found that the  $V_p/V_s$  ratio systematically increases with the increase of crustal thickness, while it decreases with the increase of crustal thickness for the Phanerozoic crust. Moreover, the average  $V_p/V_s$  ratios of Precambrian crust obtained from the studies mentioned above have considerable discrepancy. Niu and James [2002] and Nair et al. [2006] obtained a mean value of 1.74 for southern African cratons, while Chevrot and van der Hilst [2000] obtained an average value of 1.76 from Australian cratons. All are significantly lower than the global value of 1.84 for shields and platforms obtained by Zandt and Ammon [1995].

### 1.3. Seismic Studies of Crustal Structure of China

[7] Many seismic studies have been conducted regarding the crustal structure of China. These include Pn and/or Sn travel-time tomography [e.g., Liang et al., 2004; Pei et al., 2004, 2007; Sun et al., 2004; Sun and Toksöz, 2006], deep seismic sounding (DSS) experiments [e.g., Cui et al., 1995; Li and Mooney, 1998; Wang et al., 2000; Wang et al., 2003; Vergne et al., 2002; Li et al., 2006; Liu et al., 2006; Zhang et al., 2005; Zhao et al., 2006; Wang et al., 2007], and P-to-S Moho converted wave analyses [e.g., Mangino et al., 1999; Ma and Zhou, 2007; Huang et al., 2008; Lou et al., 2008; Li et al., 2009] at different scales and resolutions. The travel-time tomographic studies show that the high Pn and Sn velocities are usually associated with stable cratons and basins such as Tarim, Junggar, Qaidam, Sichuan, and Ordos [Liang et al., 2004; Pei et al., 2007; Sun and Toksöz, 2006], whereas the low velocities are located beneath areas of active volcanoes (e.g., Myanmar and western Yunnan), active seismic zones (e.g., “N-S seismic belt”), and the central Tibetan Plateau [Liang et al., 2004; Pei et al., 2004, 2007]. As part of the tomographic inversion, Moho depths were also determined [Liang et al., 2004; Sun et al., 2004; Sun and Toksöz, 2006]. Over the last decades, many DSS experiments were conducted with active sources to image crustal structure in various regions in China. About 90 seismic refraction and reflection profiles with a cumulative length of more than 60,000 km have been acquired in China. Li et al. [2006] compiled most of the crustal models derived from these seismic profiles, and constructed a contour map of crustal thickness and velocity models in 14 major tectonic regions across China.

[8] While travel-time tomography provides an effective way to image lateral heterogeneities in the crust and mantle, its resolution on Moho depth is relatively low, usually on the order of 10 km [Sun and Toksöz, 2006]. DSS data offer the desired depth resolution of crustal structure, but the high cost of data acquisition makes it difficult to reach a reasonable lateral coverage of the entire country. Moreover, the S wave velocity is poorly constrained in the DSS studies because of the lack of shear wave energy in active sources.

[9] With the rapid expansion of broadband seismic networks in recent years, receiver function analysis has emerged

to be a reliable technique to estimate thickness and  $V_p/V_s$  ratio of the Earth's crust beneath seismic stations. It has been widely applied in the major continents of the world, such as North America [e.g., Clarke and Silver, 1993; Owens et al., 1984; Ammon and Zandt, 1993; Langston, 1994; Zhu and Kanamori, 2000], South America [e.g., Niu et al., 2007], Africa [e.g., Nguuri et al., 2001; Niu and James, 2002; Nair et al., 2006], and Australia [e.g., Clitheroe et al., 2000; Chevrot and van der Hilst, 2000]. Waveform data based receiver function studies on a countrywide scale for China have been generally limited to the sparse Global Seismologic Network (GSN) deployed in this country. For example, Mangino et al. [1999] obtained six crustal velocity models by inverting receiver functions recorded by the GSN stations in China. However, their models were limited by a small number of waveforms (typically only five or six receiver functions were available per stack). On the other hand, a large number of regional studies have been conducted mainly in the tectonically active Tibetan Plateau and the Tian Shan region [e.g., Owens and Zandt, 1997; Bump and Sheehan, 1998; Mahdi and Pavlis, 1998; Wolfe and Vernon, 1998; Kind et al., 2002; Sherrington et al., 2004; Wittlinger et al., 2004; Mitra et al., 2005]. The data sources of those regional studies are usually from temporarily deployed seismic networks, such as the International Deep Seismic Sounding of Tibet and Himalayas (INDEPTH) project. Also, there are substantial discrepancies in crustal thickness estimated by different studies, even beneath the same region. For example, the receiver-function models obtained by Mitra et al. [2005] suggested that the thickest crust occurs below the Lhasa block, and reaches to approximately 88 km in depth. Other authors, however, favor the thickest crust to be about 10–20 km thinner than this value [e.g., Owens and Zandt, 1997; Kind et al., 2002]. Owens and Zandt [1997] revealed a northward thinning of the crust and an increase in  $V_p/V_s$  ratio, from about 1.78 to 1.99 which they interpreted as partial melting of the lower crust beneath northern Tibet. However, no substantial difference in crustal  $V_p/V_s$  ratio is found between northern and southern Tibet in INDEPTH III images presented by Kind et al. [2002].

## 2. Data and Method

### 2.1. Teleseismic Data of CNDSN

[10] Since the late 1990s, the China Earthquake Administration (CEA) has spent tremendous effort in building a modern digital seismic network at national level. The Chinese National Digital Seismic Network (CNDSN) is currently composed of 48 broadband stations, and has been accumulating a large amount of high-quality waveform data suitable for all sorts of scientific studies. We used teleseismic waveform data recorded at all 48 CNDSN stations to conduct a comprehensive receiver function analysis in this study. These 48 stations (including the 11 GSN stations) are evenly distributed over the entire country with an average spacing of 500–600 km between stations (Figure 2).

[11] The broadband waveforms data were provided by the China Earthquake Network Center (CENC) except for the 11 GSN stations. The data set at each station used in this study consists of approximately 350 three-component seismograms with clear direct P wave arrivals in the distance range of 30°–100° within a 4.5 year recording period. To



**Table 1.** Results of the Moho Depth,  $V_p/V_s$  Ratio (Poisson's Ratio), and the Average Crustal  $V_p$  Used in  $H-\kappa$  Search and Their Sources<sup>a</sup>

Station Code	Receiver Functions	Moho (km)	$V_p/V_s$	$\sigma$	$V_p$ (km)	$V_p$ Source
<i>NEC</i>						
HEH	278	32.3 ± 0.3	1.746 ± 0.012	0.256 ± 0.005	6.5361	TOMO
BNX	243	31.0 ± 0.5	1.732 ± 0.018	0.250 ± 0.008	6.5254	TOMO
MDJ	696	37.7 ± 0.3	1.740 ± 0.019	0.253 ± 0.008	6.4514	TOMO
CN2	26	29.3 ± 0.2	1.776 ± 0.006	0.268 ± 0.002	6.5453	TOMO
HIA	505	35.1 ± 0.6	1.652 ± 0.023	0.211 ± 0.013	6.4010	TOMO
XLT	277	35.4 ± 0.8	1.770 ± 0.010	0.266 ± 0.004	6.2367	TOMO
<i>NCB</i>						
SNY	246	31.6 ± 0.3	1.758 ± 0.017	0.261 ± 0.007	6.4194	TOMO
DL2	231	35.1 ± 0.5	1.716 ± 0.020	0.243 ± 0.009	6.2400	CRUST5.1
TIA	298	32.1 ± 0.5	1.728 ± 0.019	0.248 ± 0.008	6.3270	TOMO
BJT	536	39.1 ± 0.5	1.810 ± 0.010	0.280 ± 0.003	6.4799	TOMO
HNS	316	31.3 ± 0.3	1.704 ± 0.014	0.237 ± 0.007	6.1720	TOMO
LYN	316	33.7 ± 0.2	1.720 ± 0.011	0.245 ± 0.005	6.1381	TOMO
TIY	316	45.6 ± 0.2	1.778 ± 0.008	0.269 ± 0.003	6.5912	TOMO
HHC	320	44.0 ± 0.3	1.714 ± 0.014	0.242 ± 0.006	6.4275	TOMO
YCH	297	47.6 ± 0.3	1.692 ± 0.014	0.232 ± 0.007	6.3451	CRUST5.1
<i>SCB</i>						
WZH	232	29.8 ± 0.3	1.878 ± 0.005	0.302 ± 0.001	6.1648	TOMO
QZH	241	28.9 ± 0.2	1.746 ± 0.007	0.256 ± 0.003	6.2210	TOMO
GZH	210	29.9 ± 0.2	1.704 ± 0.011	0.237 ± 0.005	6.2721	TOMO
SZN	186	29.8 ± 0.4	1.692 ± 0.018	0.232 ± 0.009	6.4124	TOMO
QIZ	237	32.0 ± 0.2	1.708 ± 0.010	0.239 ± 0.005	6.2792	TOMO
SSE	331	32.3 ± 0.4	1.692 ± 0.016	0.232 ± 0.008	6.2281	TOMO
NJ2	166	30.7 ± 0.4	1.718 ± 0.007	0.244 ± 0.003	6.2486	TOMO
HEF	201	33.5 ± 0.3	1.724 ± 0.010	0.246 ± 0.004	6.2015	TOMO
WHN	242	31.9 ± 0.3	1.734 ± 0.012	0.251 ± 0.005	6.2218	TOMO
NNC	198	31.3 ± 0.7	1.552 ± 0.032	0.145 ± 0.025	6.2323	CRUST5.1
CNS	251	30.7 ± 0.5	1.636 ± 0.020	0.202 ± 0.012	6.2005	TOMO
GUL	236	30.6 ± 0.2	1.718 ± 0.006	0.244 ± 0.003	6.1888	TOMO
XAN	621	38.3 ± 0.5	1.662 ± 0.020	0.216 ± 0.011	6.5936	TOMO
ENH	436	46.2 ± 0.2	1.748 ± 0.006	0.257 ± 0.002	6.0309	TOMO
CD2	21	52.3 ± 0.3	1.678 ± 0.004	0.225 ± 0.002	6.3280	CRUST5.1
GYA	240	38.5 ± 0.2	1.626 ± 0.006	0.196 ± 0.004	6.0714	TOMO
PZH	244	42.9 ± 0.1	1.902 ± 0.005	0.309 ± 0.001	6.4850	TOMO
KMI	766	44.1 ± 0.3	1.705 ± 0.015	0.238 ± 0.007	6.3304	CRUST5.1
<i>NWC</i>						
LZH	837	51.8 ± 0.5	1.740 ± 0.014	0.253 ± 0.006	6.5464	TOMO
GTA	274	50.7 ± 0.6	1.694 ± 0.017	0.233 ± 0.008	6.3210	CRUST5.1
AXX	277	48.8 ± 0.5	1.736 ± 0.011	0.252 ± 0.005	6.1587	CRUST5.1
HTA	201	51.8 ± 0.4	1.752 ± 0.011	0.258 ± 0.004	6.1587	CRUST5.1
WMQ	841	45.3 ± 0.2	1.845 ± 0.013	0.292 ± 0.004	6.4393	TOMO
WUS	164	48.6 ± 0.1	1.804 ± 0.004	0.278 ± 0.001	6.5591	TOMO
KSH	166	60.3 ± 0.5	1.816 ± 0.012	0.282 ± 0.004	6.1587	CRUST5.1
<i>Tibetan</i>						
TNC	31	39.0 ± 0.2	1.568 ± 0.007	0.157 ± 0.005	6.6001	TOMO
HTG	54	56.0 ± 0.3	1.744 ± 0.009	0.255 ± 0.004	6.6651	TOMO
GOM	165	65.6 ± 0.3	1.726 ± 0.007	0.247 ± 0.003	6.4725	CRUST5.1
CAD	138	71.5 ± 0.1	1.696 ± 0.005	0.234 ± 0.002	6.3210	CRUST5.1
SQH	102	70.2 ± 0.1	1.762 ± 0.003	0.262 ± 0.001	6.4750	CRUST5.1
LSA	822	79.9 ± 0.3	1.730 ± 0.008	0.249 ± 0.003	6.3988	CRUST5.1
NAQ	110	78.3 ± 0.4	1.696 ± 0.009	0.234 ± 0.004	6.4725	CRUST5.1

<sup>a</sup>NEC, Northeast China; NCB, North China Block; NWC, Northwest China.

were used for the purpose of robust measurements. We chose the iterative deconvolution procedure in time domain proposed by *Niu and Kawakatsu* [1996] and *Ligorria and Ammon* [1999] to calculate individual receiver functions at each station. Compared to the widely used “water-level” deconvolution technique in frequency domain, this method can produce more stable results for low SNR data, but at the price of longer computation times. It is also free of complex relationships between water-level values and the resulting receiver functions.

[14] We did not perform strict data quality control on the raw waveform data in order to allow as many waveforms as possible to be used in constraining crustal structure. However, we took special care on the resulting receiver functions to eliminate noisy events caused by any reasons, especially

when we have the luxury of operating with a large number of waveforms. We took a statistical approach to select coherent receiver functions [*Tkalčić et al.*, 2006]. First, we calculated matrices of cross-correlation coefficients for each pair of radial receiver functions. Then we grouped those receiver functions whose pair cross-correlation coefficients pass a predetermined criterion ( $cc \geq 85\%$  for most cases) into one cluster. If different clusters are well coherent with each other, i.e., the pair cross-correlation coefficients of receiver functions in two clusters pass a lower criterion ( $cc \geq 80\%$  for most cases), they were further combined into one cluster. Receiver functions that are either noisy or with errors due to instrumental malfunction were found not to be able to merge into any clusters and they were consequently eliminated. Although we posted such a strict criterion in

data selection, we still found that most stations had approximately 100–300 individual receiver functions that pass the criterion (Table 1). Almost every station had excellent data quality. The only exception is station XSA, probably due to the fact that it is an island station and had power-related malfunctions which led to a very low uptime rate.

### 2.3. Improved $H - \kappa$ Stacking Method

[15] We conducted the so-called  $H - \kappa$  (crustal thickness and  $V_p/V_s$  ratio) domain search to measure these two parameters that characterize crustal structure [Zhu and Kanamori, 2000; Chevrot and van der Hilst, 2000; Niu and James, 2002; Nair et al., 2006]. The  $H - \kappa$  search technique maps velocity analysis with depth stacking. It stacks receiver functions along the travel-time curves of  $P$ -to- $S$  converted phase and two Moho reverberation phases calculated from the assumed  $H$  and  $\kappa$ . More specifically, the stacked amplitude is defined as

$$s(H, \kappa) = \frac{1}{N} \sum_i^N [\omega_1 r_i(t_1) + \omega_2 r_i(t_2) - \omega_3 r_i(t_3)]. \quad (2)$$

Here  $N$  is the number of receiver functions at a given station,  $r_i(t)$  represents the amplitude of the  $i$ th receiver functions at the predicted arrival times of the primary  $P$ -to- $S$  converted phase  $0p1s$  ( $t_1$ ), and crustal multiples  $2p1s$  ( $t_2$ ) and  $1p2s$  ( $t_3$ ). Following Niu and James [2002], we used the notation of  $npms$ , where  $n$  and  $m$  are the numbers of  $P$  and  $S$  wave legs within the crust, respectively. Considering the negative polarity of phase mode  $1p2s$ , we assigned a negative sign to it in the summation.  $\omega_1$ ,  $\omega_2$ , and  $\omega_3$  are the weighting factors. This stacking technique has the advantage of correctly calculating the moveouts of the  $P$ -to- $S$  phase and Moho reverberation phases, which consequently leads to a constructive stacking of the three phases.

[16] For any given pair of  $H$  and  $\kappa$ , the travel time  $t_1$  of  $0p1s$  relative to  $P$  wave was calculated using the following equation by assuming a single-layer crust model with an average velocity  $V_p$ , thickness  $H$ , and a constant  $V_p/V_s$  ratio  $\kappa$ :

$$t_1 = H \left[ \sqrt{\left(\frac{\kappa}{V_p}\right)^2 - p^2} - \sqrt{\left(\frac{1}{V_p}\right)^2 - p^2} \right], \quad (3)$$

where  $p$  is the  $P$  wave ray parameter in s/km. We calculated  $p$  for each event station pair on the basis of the global AK135 velocity model. Similarly,  $t_2$  and  $t_3$  were calculated by

$$t_2 = H \left[ \sqrt{\left(\frac{\kappa}{V_p}\right)^2 - p^2} + \sqrt{\left(\frac{1}{V_p}\right)^2 - p^2} \right], \quad (4)$$

$$t_3 = 2H \sqrt{\left(\frac{\kappa}{V_p}\right)^2 - p^2}, \quad (5)$$

[17] We searched the optimal combination of  $H$  and  $\kappa$  that gives the maximum amplitude of the  $s(H, \kappa)$ . However,

there always exists a trade-off between  $H$  and  $\kappa$  through the  $H - \kappa$  domain. As Nair et al. [2006] demonstrated, when only a single phase,  $0p1s$ ,  $2p1s$ , or  $1p2s$ , is used, there is a complete trade-off between  $H$  and  $\kappa$ , which results in multiple pairs of  $H$  and  $\kappa$  that gives the acceptable amplitude peaks in  $s(H, \kappa)$ . This trade-off can be partially resolved by combining the three phases with different weights as expressed in equation (2). For example, Zhu and Kanamori [2000] employed [0.7, 0.2, 0.1] for phases  $0p1s$ ,  $2p1s$ , and  $1p2s$ , respectively, in measuring Moho depth in southern California; Chevrot and van der Hilst [2000] used [0.5, 0.5, 0.0] in estimating the Poisson's ratio of Australian crust; Nair et al. [2006] employed [0.5, 0.3, 0.2] in constraining crustal structure of southern Africa. This technique is, however, not efficient enough to eliminate the trade-off between  $H$  and  $\kappa$ , which leads to a “band” area of amplitude peak in  $H$  and  $\kappa$  domain map (Figure 3a). It becomes more challenging to apply this technique to areas underlain by thick crust with complicated structure such as the west of China, where phases related to crustal layers can be easily misidentified as Moho reverberations. We developed a new technique to stabilize the  $H - \kappa$  domain search by calculating the coherence between the  $P$ -to- $S$  conversion and the reverberation phases at different  $\kappa$  values. Specifically, we performed the time to depth conversion for each  $\kappa$  for three different modes: The primary  $P$ -to- $S$  conversion  $0p1s$  mode, the reverberations  $1p2s$  and  $2p1s$  modes. We then calculated the semblance,  $c(\kappa)$ , of the three traces around the peak of the  $0p1s$  trace and used it as the weighting factor. If the assumed  $\kappa$  is correct, the three depth traces are expected to correlate well with each other around the maximum conversion depth [Niu et al., 2007]. The  $H - \kappa$  stacking is thus modified to be

$$s(H, \kappa) = \frac{c(\kappa)}{N} \sum_i^N [\omega_1 r_i(t_1) + \omega_2 r_i(t_2) - \omega_3 r_i(t_3)]. \quad (6)$$

[18] We assign weights [0.50, 0.25, 0.25] for phase modes  $0p1s$ ,  $2p1s$ , and  $1p2s$ , respectively. As illustrated on Figure 3b, this technique is able to efficiently eliminate the effect of trade-off between  $H$  and  $\kappa$ . The “band” area shown in Figure 3a disappeared, and the amplitude contour is more focused on the global maximum. We also employed the  $n$ th-root ( $n = 4$ ) technique in the stacking to reduce the uncorrelated noise [Niu and James, 2002].

## 3. Results

### 3.1. Crustal Thickness and $V_p/V_s$ Ratio Measurements

[19] We performed crustal thickness and  $V_p/V_s$  ratio measurements on all 48 CNDSN stations using the enhanced  $H - \kappa$  domain search technique. The method was applied on both  $R/Z$  and  $S/P$  receiver functions. For the stations located at stable areas, both results were very similar, and we chose to show  $S/P$  receiver functions (Figure 3c). However, as we mentioned above (section 2.2), for those stations located above a thick sedimentary layer, the calculated incidence angle does not reflect the true one. Consequently, the  $P/SV$  projection does not necessarily reduce much  $P$  wave energy in the resulting receiver functions. In this case we still used  $R/Z$  receiver functions. In principle, as long as the arrival time of the primary  $P$ -to- $S$  converted wave is robustly picked, one

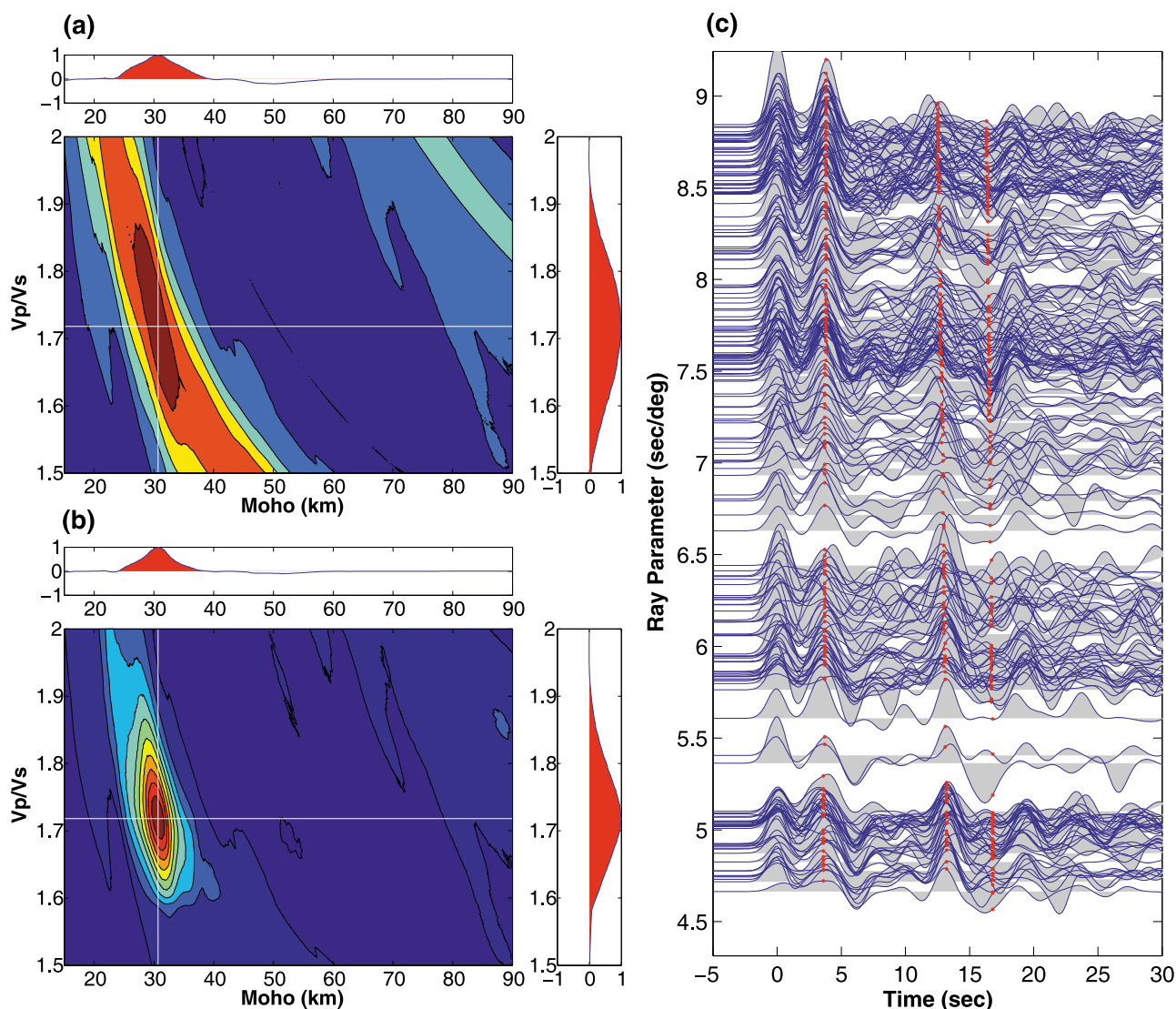


**Figure 3.** Result of “ $H - \kappa$ ” domain search for receiver functions generated from the  $P/SV$  components recorded at station GUL. (a) Contour map of the summed amplitude as a function of crustal thickness and  $V_p/V_s$  ratio using the conventional “ $H - \kappa$ ” technique. (b) The same as Figure 3a, but using the modified techniques. The large band area due to the trade-off between  $H$  and  $\kappa$  shown in Figure 3a shrinks to a small area in Figure 3b. (c) Receiver function traces sorted by ray parameters. The red dots on each receiver function indicate the predicted arrival times of  $0p1s$ ,  $2p1s$ , and  $1p2s$ , respectively, calculated using the optimal crustal thickness and  $V_p/V_s$  ratio.

can estimate Moho depth with an assumed velocity model. In order to determine  $V_p/V_s$  ratio, however, it is critical to have clear multiples on the receiver functions, which may not always be true. The calculation of cross-correlation coefficients  $c(\kappa)$  between the three phases  $0p1s$ ,  $2p1s$ , and  $1p2s$  facilitates the identification of the two multiples. We accepted the measurements only when the coefficients are of consistently high quality to ensure reliable estimation for  $V_p/V_s$  ratios. In practice, after locating the optimal  $H$  and  $\kappa$  pair at each station, we further checked the receiver functions to confirm whether the three phases are correctly identified and are consistent with respect to the optimal  $H$  and  $\kappa$  pair (Figure 3c).

[20] The stacked  $s(H, \kappa)$  at 47 stations out of the total 48 CNDNSN stations are shown in Figure 4 and the measured

Moho depths and  $V_p/V_s$  ratios are listed in Table 1. The waveforms recorded at the island station XSA are so noisy that we were not able to obtain reliable measurements for both crustal thickness and  $V_p/V_s$  ratio. In Figure 4 and Table 1, stations are sorted by tectonic regions: Northeast China (NEC), North China Block, South China Block, Northwest China (NWC), and the Tibetan Plateau (Figure 2). We will discuss these results in detail in sections 4.1–4.5. We calculated  $1\sigma$  errors for the measurements of Moho depth and  $V_p/V_s$  ratio on the basis of a bootstrap method [Efron and Tibshirani, 1986]. Here one should note that these formal errors do not include any uncertainty in the reference velocity model. So the actual errors could be larger than our estimates.

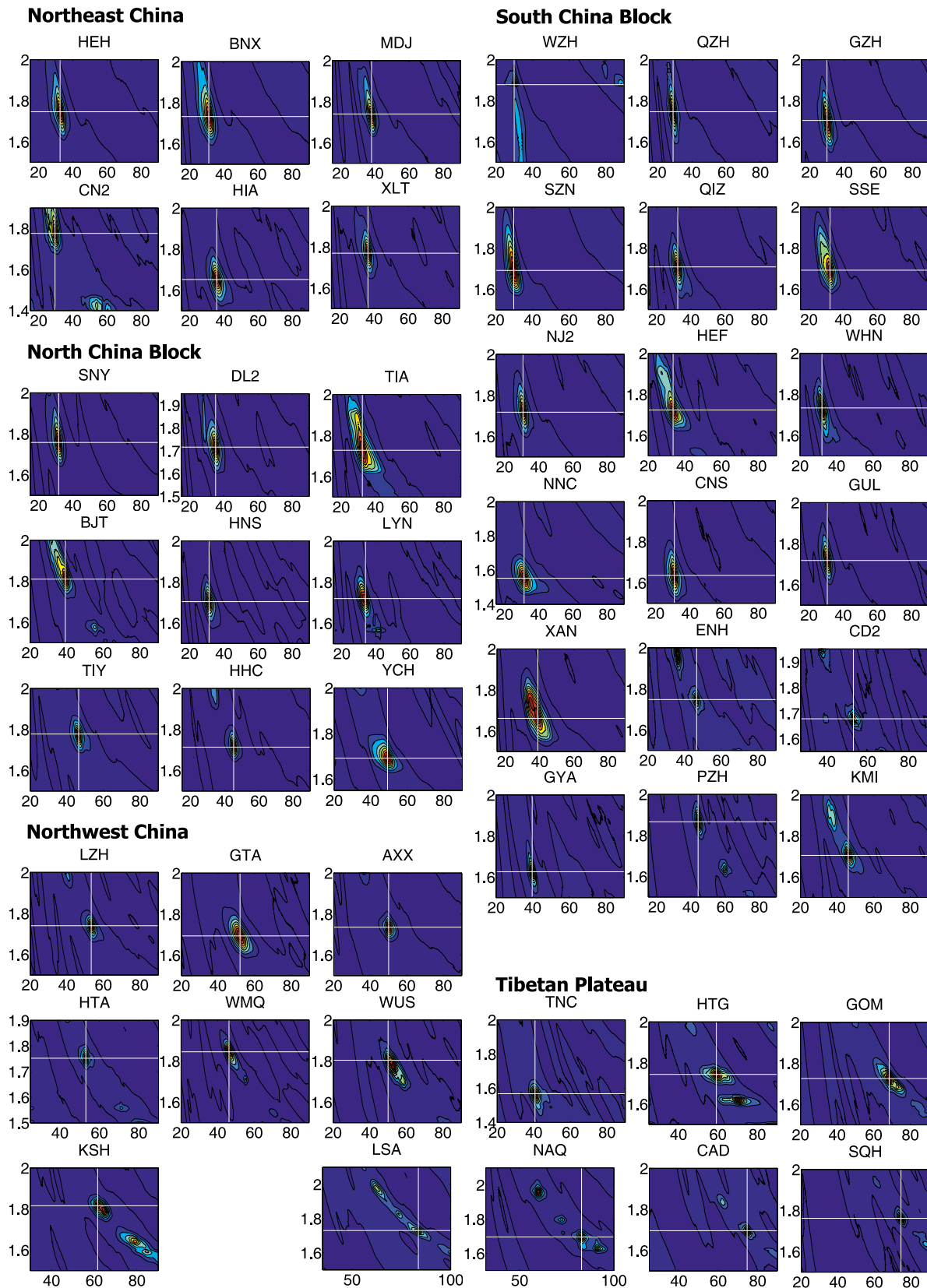


**Figure 4.** Crustal thickness and  $V_p/V_s$  ratio measurements of the 47 CNDSN stations. The optimal crustal thickness and  $V_p/V_s$  ratio are identified from the cross point of the two white lines. The results are organized on the basis of the five tectonic regions described in context.

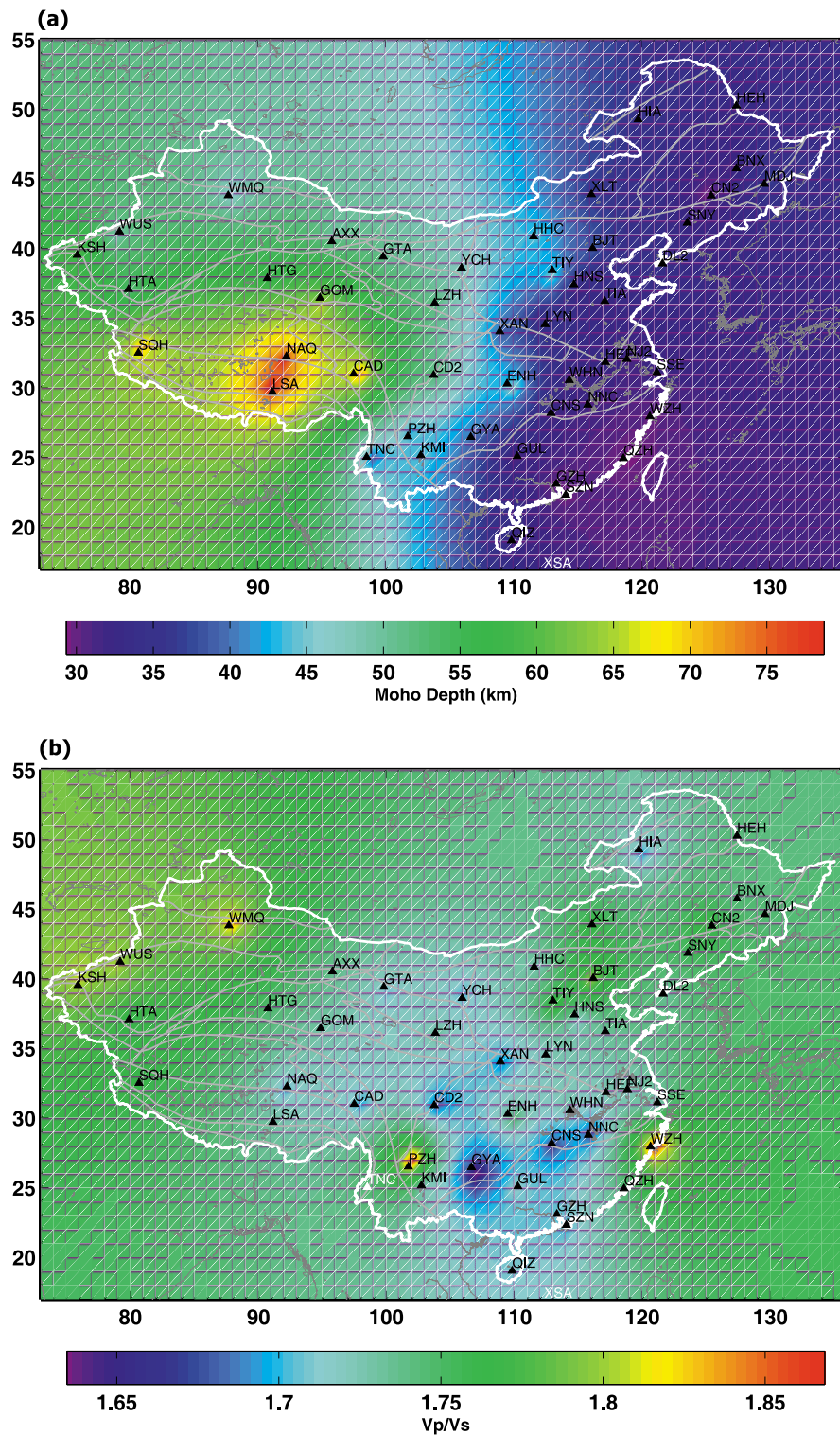


**Figure 5.** (a) Moho relief map inverted from observations on stations shown as black triangles. An inversion was performed to minimize the lateral variation of Moho depth (see *Niu et al.* [2007] for details). (b) Map of lateral variations for  $V_p/V_s$  ratio. The inversion method is the same as that used for the Moho relief map (Figure 3a). Results on stations TNC and XSA are not used in the inversion. Note that the margins outside station coverage in both maps are poorly constrained.

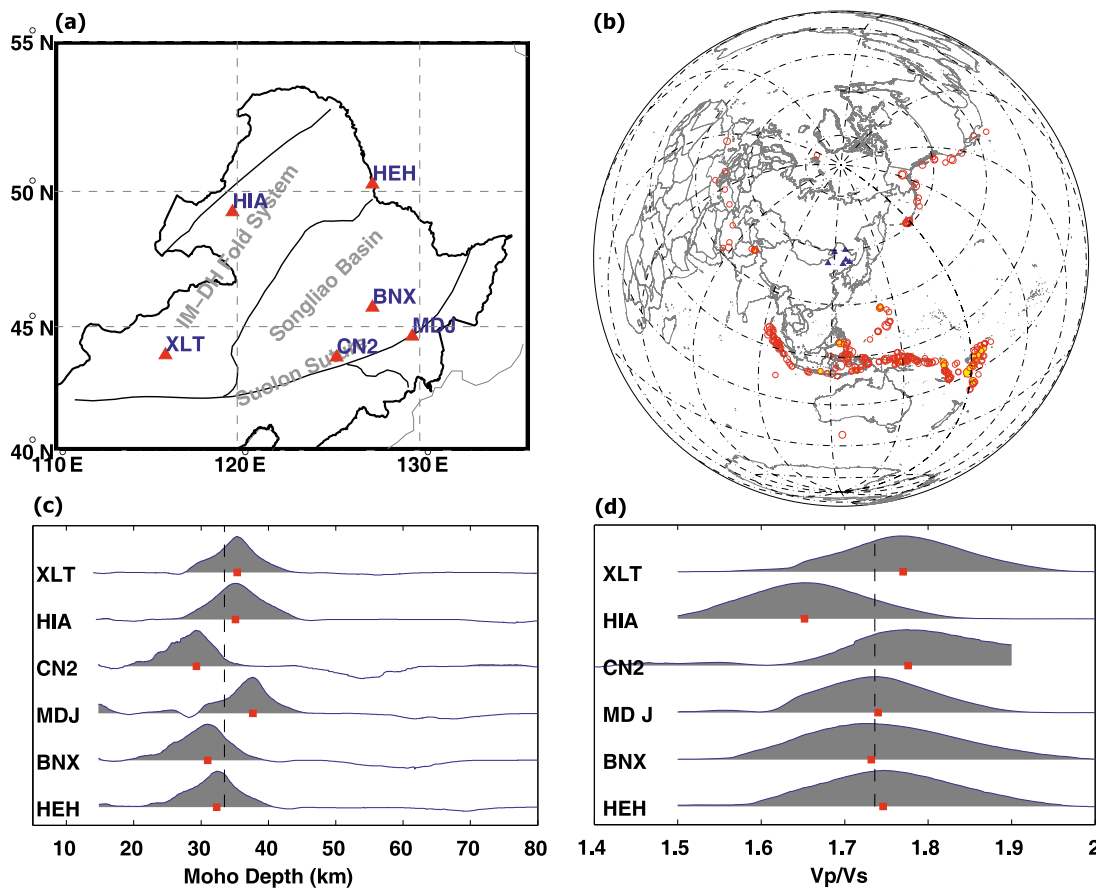


**Figure 6.** The results of stations in NEC. (a) The map of this subregion that shows the locations of analyzed stations (triangles) and main tectonic features. (b) Distribution of teleseismic events (dots) used in the six stations in this subregion. The exact events and the number of events may be slightly different for individual stations. (c) Stacked receiver functions are mapped to depth. The squares denote the maximum peak corresponding to the depth of Moho. (d) The same as Figure 6c but for  $V_p/V_s$  ratios.

### 3.2. Robustness of Measurements

[21] There are three unknown parameters,  $V_p$ ,  $H$ , and  $\kappa$  in equations (3)–(5). It can be shown from those equations that the estimated Moho depth strongly depends on the selection of  $V_p$  while the  $V_p/V_s$  ratio is almost insensitive to  $V_p$ . In principle, the average crustal velocity  $V_p$  can be constrained through the so-called velocity analysis technique if the data provide a good coverage in epicentral distance [e.g., *Gadallah and Fisher, 2005*]. Because of the highly uneven distribution of earthquakes, we found that the teleseismic distance range to the CNDSD stations cannot provide sufficient coverage in ray parameter space that is required for velocity analysis. We thus used an a priori knowledge of crustal velocity to conduct the “ $H - \kappa$ ” domain search. We employed a tomographic velocity model derived from  $Pn$  travel times [*Sun and Toksöz, 2006*] (tagged with TOMO in Table 1). The model has a horizontal resolution of  $1^\circ \times 1^\circ$  and vertical resolution of 10 km. For stations where the 3-D tomographic model is unavailable, we used CRUST 5.1 [*Mooney et al., 1998*] to construct a 1-D reference velocity model (tagged with CRUST5.1 in Table 1). Although we did not include errors from the unmodeled velocity structure in the Moho depth measurements, such errors should be of the same order as the uncertainties in the velocity

models. For regions where both velocity models are available, we found that the average velocity calculated from the two models has a difference  $<5\%$  in most regions, and about 7% within the Tibetan terranes and the Sanjiang fold belts in southwestern part of China. This corresponds to an uncertainty of about 6%–8% in the resulting  $H$ . As mentioned above, errors of several percent in velocity model have almost no effect on the  $V_p/V_s$  ratio. This is consistent with the conclusions from previous studies [e.g., *Clarke and Silver, 1993; Zhu and Kanamori, 2000*].

[22] In general, lateral velocity heterogeneities in the crust beneath the area surrounding a station result in incoherent stacking which could significantly reduce the stacked amplitude of the three phases. For instance, on the basis of equations (3)–(5), for a Moho at 35 km and a  $P$  wave ray parameter  $p = 6.5$  s/deg, a lateral velocity variation of 5% leads to a change of 0.19 s in  $t_1$ , 0.77 s in  $t_2$ , and 0.96 s in  $t_3$ . Since we adopted a low-pass Gaussian filter ( $a = 1.0$  rad/s) in computing receiver functions, these variations in travel time are still smaller than half of the dominant period of the converted phases. Thus, at most stations lateral heterogeneities are unlikely to have significant effects on the stacking amplitude. However, we did observe substantial variations among individual receiver functions for some

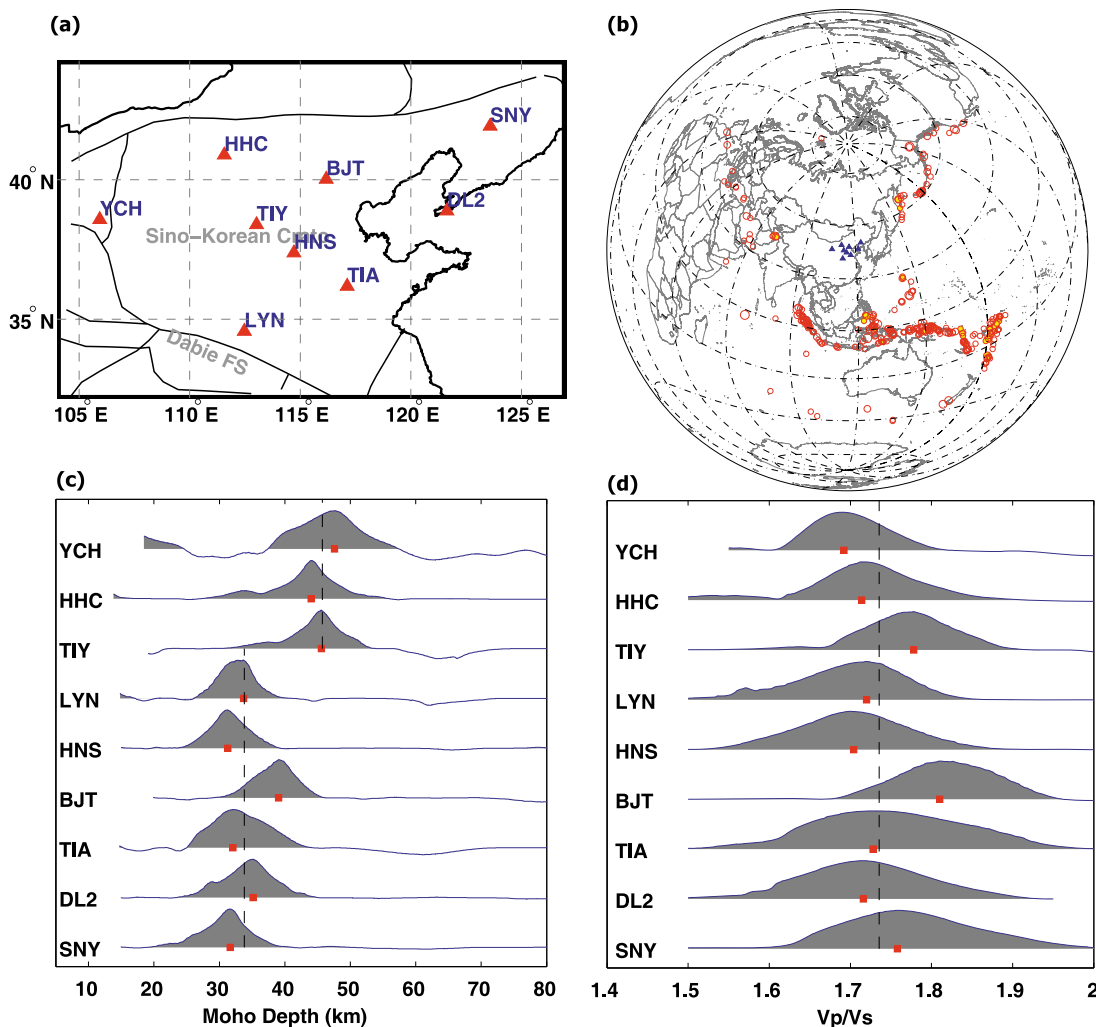


**Figure 7.** The results of stations in NCB. (a) The map of this subregion that shows the locations of analyzed stations (triangles) and main tectonic features. (b) Distribution of teleseismic events (dots) used in the nine stations in this subregion. The exact events and the number of events may be slightly different for individual stations. (c) Stacked receiver functions are mapped to depth. The squares denote the maximum peak corresponding to the depth of Moho. (d) The same as Figure 7c but for  $V_p/V_s$  ratios.

stations such as CN2, CD2, and TNC. The lateral velocity changes surrounding these stations thus could be greater than 5% if they are the main causes of the incoherency.

### 3.3. Distribution of Moho Depth and $V_p/V_s$ Ratio

[23] We use 47 Moho depth and 46  $V_p/V_s$  ratio measurements to generate 2-D relief maps for Moho depth and  $V_p/V_s$  ratio, respectively (Figures 5a and 5b). We divided the study area from 17°N to 55°N in latitude and 73°E to 136°E in longitude into meshed grids of 1° × 1°. The total 2496 (39 × 64) unknown parameters of Moho depth were inverted from 47 observations. The kernel matrix has a dimension of 47 × 2496 with 47 nonzero elements (= 1) that correspond to the 47 observations. A regularization that minimizes the first derivative of the model (the flattest Moho) is added to constrain the underdetermined inversion. Details of this algorithm were described by *Niu et al.* [2007]. Similar to Moho depth, we also inverted a 1° × 1°  $V_p/V_s$  model from the 46 measurements (Figure 5b). We must note here that the main purpose to generate the 2-D

maps is to demonstrate lateral variations of Moho depth and  $V_p/V_s$  ratio across China. The actual resolution is less than the 1° × 1° grid in our map. Moreover, our data have no resolution in the corner regions at all, thus they may not reflect the true values of the Moho depth and  $V_p/V_s$  ratio.

[24] The resultant Moho map presents a highly variable crustal structure across China. The most prominent feature shown in this map is the existence of an apparent “N-S trending belt” between about 100°E and 110°E which divides the crust beneath China into two parts in the EW direction. The crust is less than 36 km thick beneath the eastern part of China. It thickens gradually toward the west and reaches to 40–49 km in central China. The south China fold belts and the eastern Yangtze craton have the thinnest crust in the whole region while the crust beneath northeast China is a few kilometers thicker. In the western part of China, the crustal thickness increases sharply across the margin of the Tibetan Plateau, probably reaching to about 80 km (corrected for topography) beneath the central part of the plateau. The mean of  $V_p/V_s$  ratios of all reliable measure-

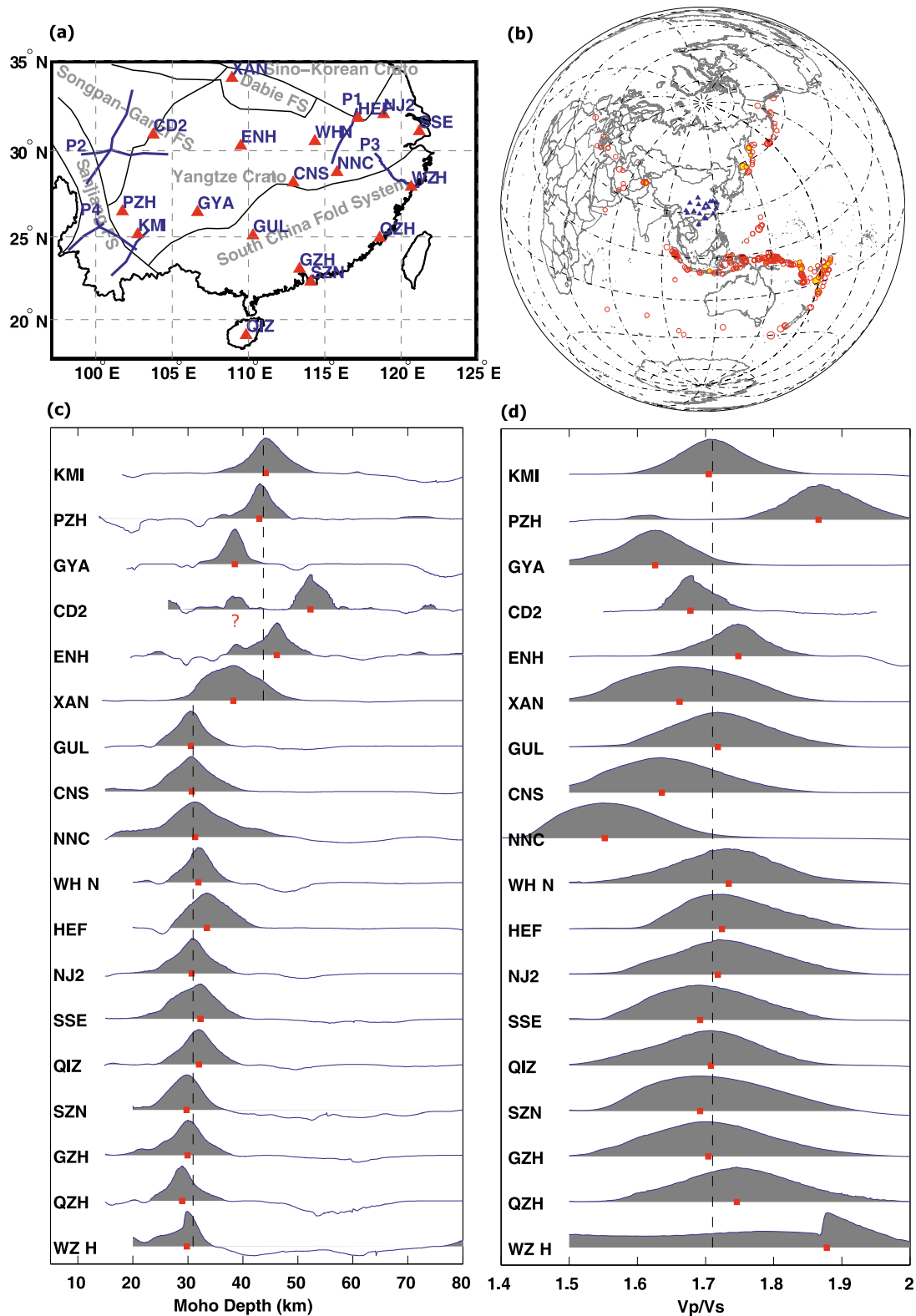


**Figure 8.** The results of stations in SCB. (a) The map of this subregion that shows the locations of analyzed stations (triangles) and main tectonic features. The deep seismic sounding (DSS) profiles that are cited in text are also displayed. (b) Distribution of teleseismic events (dots) used in the 18 stations in this subregion. The exact events and the number of events may be slightly different for individual stations. (c) Stacked receiver functions are mapped to depth. The squares denote the maximum peak corresponding to the depth of Moho. The question mark on CD2 indicates another strong velocity jump in the crust beneath the station. The vertical lines indicate the group means. (d) The same as Figure 8c but for  $V_p/V_s$  ratios.

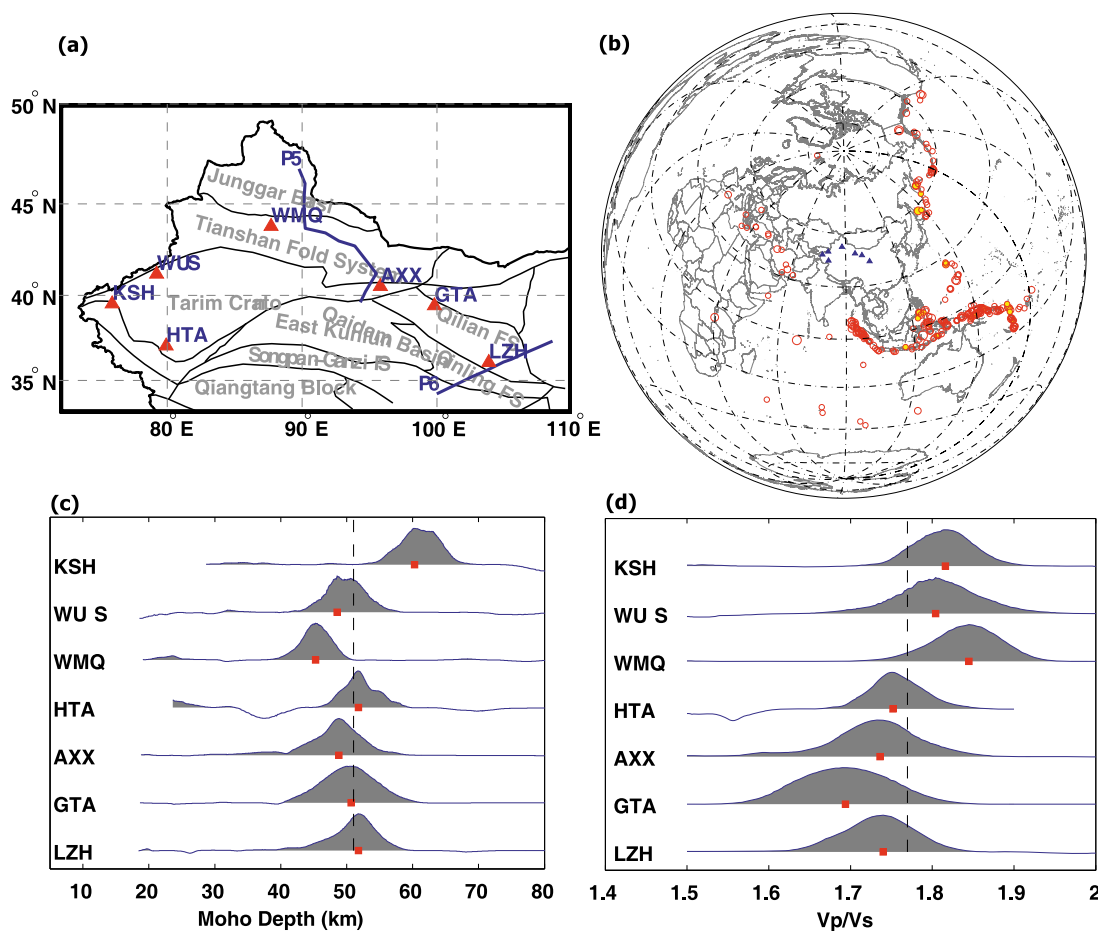


**Figure 9.** The results of stations in NWC. (a) The map of this subregion that shows the locations of analyzed stations (triangles) and main tectonic features. The DSS profiles that are cited in text are also displayed. (b) Distribution of teleseismic events (dots) used in the seven stations in this subregion. The exact events and the number of events may be slightly different for individual stations. (c) Stacked receiver functions are mapped to depth. The squares denote the maximum peak corresponding to the depth of Moho. (d) The same as Figure 9c but for  $V_p/V_s$  ratios.

ments in China is about 1.73, lower than the global average of 1.78 for the bulk continental crust [Zandt and Ammon, 1995], which may indicate a general absence of a mafic lowermost crustal layer across the entire area of mainland China. The Yangtze craton has a lower  $V_p/V_s$  ratio than the other two major cratons in China, the Sino-Korean and the Tarim craton.

#### 4. Discussion

[25] We organized the results of receiver function measurements into the following five large tectonic and physiographic regions on the basis of the location of the stations: (1) Northeast China (NEC). It is basically a part of the Mongolia accretionary fold belt, and joined with the North China craton along the Suolon suture (Figure 6a); (2) North China Block (NCB). It is also known as the Sino-Korean Craton, which consists of an Archean (older than 2.5 Ga) continental nuclei and the surrounding Paleoproterozoic (about 1.8 Ga) orogenic belts (Figure 7a); (3) South China Block (SCB). It refers to the Yangtze craton and the Precambrian Cathaysia block. The Cathaysia block consists of one

part known as the south China fold belt and another part that lies underwater east of the fold belt (Figure 8a); (4) Northwest China (NWC). We assign various tectonic blocks such as the Tarim-Qaidam block, the Tian Shan fold system, and the Junggar block in the vast western China to this group (Figure 9a); (5) The Tibetan Plateau. Large areas in the southwestern and central China are assigned to this group. Specifically, it includes the Himalaya block, Lhasa block, Qiangtang block, Sanjiang fold system, Songpan-Ganzi fold system, and part of the Kunlun-Qaidam-Qilian Shan tectonic block (Figure 10a).

[26] We have to note here that such division is somewhat arbitrary. For example, both Northeast China and Northwest China belong to the northern accretionary complexes and post-Paleozoic intracontinental fold belts, but we divided it into two tectonic regions for the convenience of discussion. We assigned stations SNY and YCH to the North China Block (Figure 7a); however, they can also be grouped to the Northeast China and Northwest China, respectively, on the basis of their locations. Some stations such as HEF which is located at the suture zone of North China Block and South China Block can be assigned to either tectonic region

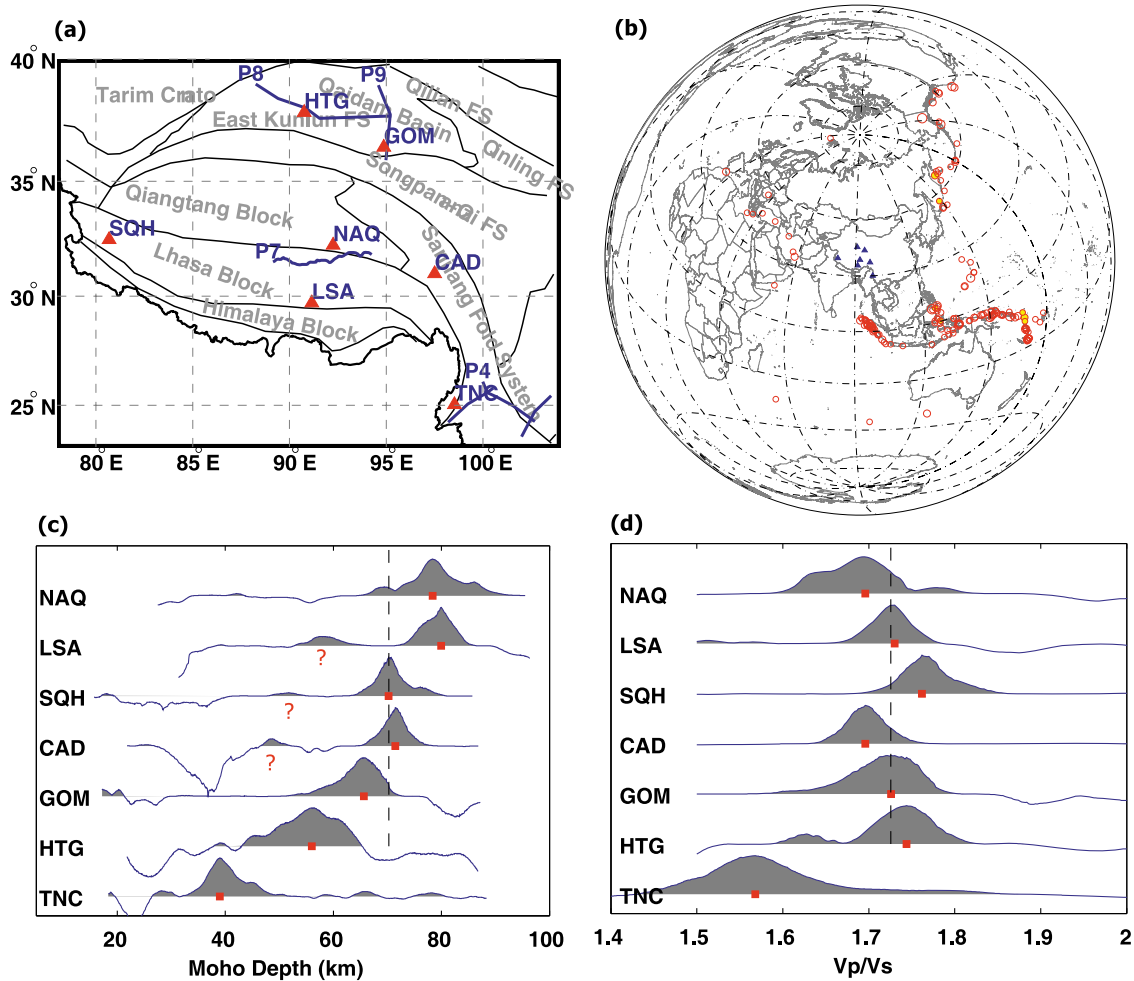


**Figure 10.** The results of stations in the subregion of Tibetan Plateau. (a) The map of this subregion that shows the locations of analyzed stations (triangles) and main tectonic features. The DSS profiles that are cited in text are also displayed. (b) Distribution of teleseismic events (dots) used in the seven stations in this subregion. The exact events and the number of events may be slightly different for individual stations. (c) Stacked receiver functions are mapped to depth. The squares denote the maximum peak corresponding to the depth of Moho. The question marks on some traces indicate another strong velocity jump in the crust beneath the stations. The vertical lines indicate the group means. (d) The same as Figure 10c but for  $V_p/V_s$  ratios.

(Figure 8a). The assignment of the stations to the five tectonic regions is listed in Table 1, along with their measured crustal thickness,  $V_p/V_s$  ratios, and the equivalent Poisson’s ratios.

**4.1. Northeast China**

[27] Six stations are deployed in this region (Figure 6a). The optimal crustal thickness and  $V_p/V_s$  ratio beneath each

station are obtained from the maximum amplitude in the  $H - \kappa$  stack (Figures 6c and 6d). The averaged crustal thickness and  $V_p/V_s$  is 33.5 km and 1.738 ( $\sigma = 0.252$ ) (Table 2), respectively. Station HIA (located on the Hulunbuir Plateau) has a lower  $V_p/V_s$  ratio than other stations in this region. If HIA is discounted, the crust beneath northeast China presents a more uniform  $V_p/V_s$  ratio of about 1.753

**Table 2.** Comparison of Crustal Thickness ( $H$ ) and  $V_p/V_s$  Ratios ( $\kappa$ ) Between Different Studies

	Receiver Functions	DSS Profiles <sup>a</sup>	Sun and Toksöz [2006]	Liang et al. [2004]
NEC	$H = 29-38; \kappa = 1.736 (\sigma = 0.252)$	$H = 32-40; \kappa = 1.770 (\sigma = 0.266)$	$H = 39-43$	$H = 36-38$
NCB	$H = 31-39, 44-48; \kappa = 1.736 (\sigma = 0.252)$	$H = 28-36, 40-46; \kappa = 1.775 (\sigma = 0.268)$	$H = 31-40, 40-46$	$H = 32-36, 40-50$
SCB	$H = 29-34, 38-46; \kappa = 1.712 (\sigma = 0.241)$	$H = 30-34, 40-46; \kappa = 1.780 (\sigma = 0.269)$	$H = 30-35, 35-44$	$H = 32-40, 40-50$
N-S Belt	$H = 40-49$	$H = 40-46$	$H = 40-46$	$H = 40-60$
NWC	$H = 45-60; \kappa = 1.770 (\sigma = 0.265)$	$H = 42-58; \kappa = 1.759 (\sigma = 0.261)$	$H = 47-54$	$H = 50-55$
Tibetan Plateau	$H = 56-80^b; \kappa = 1.726 (\sigma = 0.247)^b$	$H = 60-74; \kappa = 1.761 (\sigma = 0.262)$	$H = 58-73$	$H = 55-65$

<sup>a</sup>Li et al. [2006] and CRUST 5.1. DSS, deep seismic sounding.

<sup>b</sup>TNC is excluded.

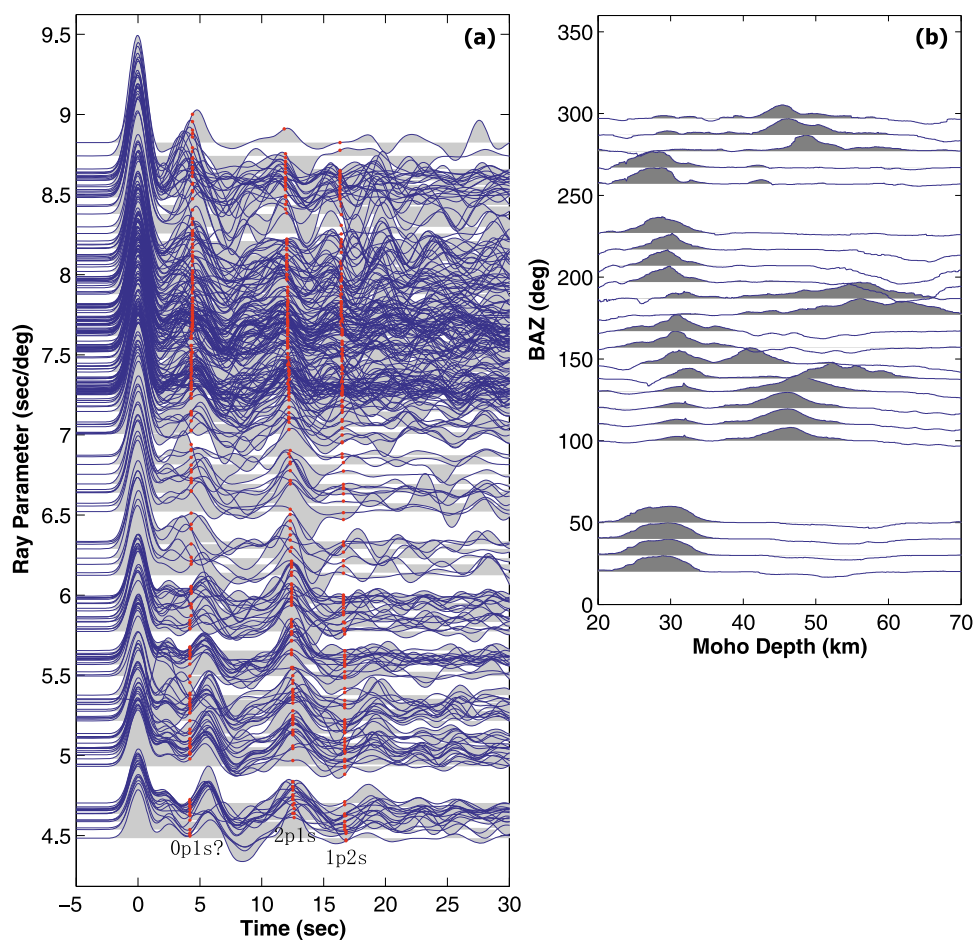


**Figure 11.** (a) Receiver functions generated from the  $R$  and  $Z$  components recorded at station CN2. The red dots on each receiver function indicate the expected arrivals of  $0p1s$ ,  $2p1s$ , and  $1p2s$  calculated from the optimal crustal thickness and  $V_p/V_s$  ratio using events from all back azimuths. The noticeable shift between the predicted and observed arrivals of  $0p1s$  in some azimuth range suggests that the crustal thickness and  $V_p/V_s$  ratio obtained from “ $H - \kappa$ ” domain search cannot reconcile receiver functions from all back azimuths. (b) Depth-stacked receiver functions generated at 23 back-azimuth bins, each of which spans  $30^\circ$ . We interpret the peaks at about 30 km as the Moho. The peaks at about 45 km on traces within  $100^\circ - 150^\circ$  and  $280^\circ - 300^\circ$  indicate strong back-azimuthal dependence of the Earth structure beneath the station if they are interpreted as Moho.

( $\sigma = 0.259$ ) with a standard deviation 0.019. In general the northwestern part of this region belongs to the Mongolia accretionary fold belt, which is a collage of Ordovician to early Permian island arcs, blueschist-bearing assemblages, Paleozoic ophiolites, and possible microcontinental blocks [Davis *et al.*, 2001]. The southeastern part is basically occupied by the Songliao basin, which may be caused by Pacific backarc extension, or by gravitational collapse of the late Paleozoic orogen [Graham *et al.*, 2001]. Seismic refraction investigation using active sources for this region showed a 36–40 km thick crust beneath the Mongolia-Hailar fold system, and a 32–34 km thick crust beneath the Songliao basin [Yuan *et al.*, 1986; Li *et al.*, 2006]. Our receiver function analysis indicated that the crustal thickness beneath the two stations, HIA and XLT, located in the Inner-Mongolia agreed well with the active source results. Both showed a Moho depth of approximately 35–36 km. However, stations located in the Songliao basin presented a broad range of crustal

thickness from 29.3 to 37.7 km. The crustal thickness and  $V_p/V_s$  ratio derived from receiver function data did not show significant difference between the ancient orogen and the basin as revealed by the previous active source studies [Li *et al.*, 2006].

[28] At station CN2, we observed systematic variations in the arrival times of the three phases as shown in Figure 11a. The dots on each receiver function trace indicate the expected arrivals of the three phase modes calculated from the optimal  $H$  and  $\kappa$  combination. The clearly identified  $P$ -to- $S$  converted phases (indicated by “ $0p1s$ ” in Figure 11a), however, significantly deviate from the expected arrival times especially at low ray parameter range. We also observed a minor positive phase prior to the  $P$ -to- $S$  phase on those receiver function traces. Such observations are probably due to a strong laterally heterogeneous structure in lower crust. To examine azimuthal dependence of crustal structure around CN2, we binned receiver functions in  $30^\circ$  back azimuth

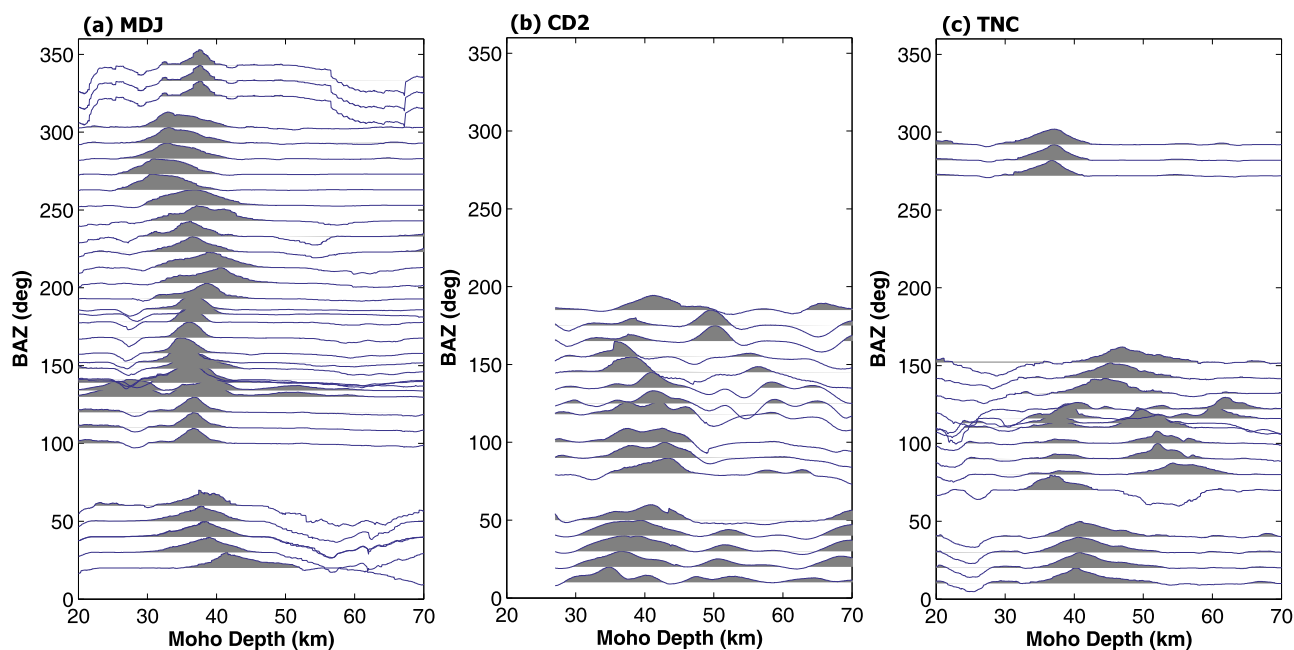


**Figure 12.** Depth-stacked receiver functions generated at back-azimuth bins for stations MDJ, CD2, and TNC, respectively.

windows and moved the window at  $10^\circ$  steps. The stacked receiver functions gathered at all back azimuthal bins are mapped to depth and shown in Figure 11b. From  $100^\circ$  to  $150^\circ$  in back azimuth, there are two peaks in the stacked receiver functions and we interpreted the deeper one with larger amplitude as the Moho.

[29] We also observed back-azimuthal dependence of Moho depth on station MDJ (Figure 12a). A wide range of estimates of crustal thickness in the vicinity of MDJ has been published. The Moho depth varies from 27 km from regional  $P$  and  $PP$  waveform modeling [Beckers *et al.*, 1994], 34–36 km by active source seismic refraction experiment [Yuan *et al.*, 1986], 42–43 km by surface wave modeling [Feng *et al.*, 1981], to 36–42 km by very few receiver functions measurements [Mangino *et al.*, 1999]. Our receiver function observation estimates an average thickness of 37.7 km. The difference between these results suggests that the crust-mantle transition occurred gradually, probably within approximately 5 km, rather than abruptly. CN2 and MDJ are located along the strike of the Suolon suture which welded the Mongolian arc terranes and the North China craton together during the late Permian and early Triassic. During the Jurassic and Cretaceous, the Suolon suture was reactivated as the Yanshan fold and thrust belt associated with the extension that formed the Hailar basin and the Songliao basin in the Mongolian arc terranes [Davis *et al.*, 2001; Graham *et al.*, 2001]. The complicated tectonic history, as well as the existence of several known and inferred faults near stations, makes it hard to estimate the average crustal structure around these stations. For CN2, we could not find an optimal crustal thickness and  $V_p/V_s$  ratio that can reconcile all the receiver functions, indicating the presence of strong lateral heterogeneities beneath the station. We thus chose events in the direction of northeast ( $30^\circ$ – $60^\circ$  in back azimuth) from which the waveforms are relatively simple

compared to those from other directions. We used the crustal thickness and  $V_p/V_s$  ratio derived from this subset of data to represent the measurements of this station since they agree with the nearby stations. If the observed back-azimuthal dependence is related to the structure of the Suolon suture, further investigations for this region are required to explain this phenomenon.

#### 4.2. North China Block

[30] The North China Block consists of a few Archean basements and widespread Proterozoic sedimentary cover. The tectonic elements include the Alashan plateau, the Ordos basin, and North China plain from the west to the east. The North China Block is bounded to the north by the Yanshan fold belt and to the south by the Qinling-Dabie fold belt which was formed by the collision with the South China Block during late Permian and Triassic [Yin and Nie, 1996]. To the southwest, the North China Block is sutured against the Qaidam block along the Qilian Shan. To the east, the Tan-Lu fault system forms the major boundary of this block.

[31] We had nine stations in this large tectonic region (Figure 7a). Receiver functions from all the stations presented prominent and coherent  $0p1s$ ,  $2p1s$ , and/or  $1p2s$  modes corresponding to the optimal crustal thickness and  $V_p/V_s$  ratio pairs. Our observations show a scenario that the crust beneath the North China Block is relative simple and there is a well-defined boundary between the crust and mantle (Figure 7c). The measured crustal thicknesses can apparently be divided into two groups. The crust beneath the six stations (SNY, DL2, TIA, BJT, HNS, and LYN) to the east has an average thickness of 33.8 km. Most of these stations are located in the North China plain. In contrast, the average thickness of the crust beneath the three stations (TIY, HHC, and YCH) to the west is 45.7 km, about 12 km thicker than

the crust to the east. The apparent thinning of crust to the east could be the result of extensional thinning of a previously thickened and unstable crust associated with the widespread development of extensional basins inside the North China Block in the Mesozoic time [Wang *et al.*, 2005].

[32] The crustal  $V_p/V_s$  ratio varies from 1.692 ( $\sigma = 0.232$ ) at YCH to 1.810 ( $\sigma = 0.280$ ) at BJT with a mean of 1.736 ( $\sigma = 0.252$ ) (Figure 7d). This value is significantly lower than the global average of the shields and platforms ( $1.81 \pm 0.04$ ) [Zandt and Ammon, 1995]. We note that Zandt and Ammon [1995] included only one station, BJT, which has a relatively high  $V_p/V_s$  ratio, from the North China craton. The  $V_p/V_s$  ratio suggests that the crustal rocks in this region are rather felsic. We speculate that the overall felsic composition is due to either the lack of a thick mafic/ultramafic layer in the lowermost crust or the thick sedimentary cover rich in silica found in this region. Li *et al.* [2006] compiled 14 representative seismic velocity-depth profiles across China and found that the North China Block has a very thin mafic (0–4 km) layer lying underneath a relatively thick felsic layer up to 10–20 km.

### 4.3. South China Block

[33] It is a relatively stable tectonic region consisting of the Yangtze craton and the Cathaysia block. Neoproterozoic granitic and mafic-ultramafic intrusions are widespread in South China, and have been attributed to continental collision between the Yangtze and Cathaysia blocks, or magmatic arc and crustal melting above a mantle plume [Li *et al.*, 1999; Zhou *et al.*, 2002].

[34] As the most important industrial and most densely populated region in China, the CNDSN deployed more stations in this region to monitor seismic activity. We had a total of 18 stations in this region (Figure 8a). Similar to the North China Block, the crustal thickness measured from the 18 stations also showed a bimodal distribution (Figure 8c). The crust to the southeast is as thin as  $31.0 \pm 1.3$  km. It includes the stations on the Cathaysia block along the coastline (WZH, QZH, GZH, SZN, and QIZ), some stations on the eastern part of the Yangtze craton (SSE, NJ2, HEF, and WHN), and some stations along the orogenic belts separating the Yangtze and Cathaysia blocks (NNC, CNS, and GUL). To the northwest, the crust thickens up to about 44.4 km. The average  $V_p/V_s$  ratio of the South China Block is 1.712 ( $\sigma = 0.241$ ) with a relatively large variation (Figure 8d). In general, the crustal structure revealed by our receiver function analysis suggests a relatively sharp, flat, and thin crust beneath the southeastern part of this block. The crustal structure becomes complicated beneath some stations to the northwest, probably as a result of local heterogeneity in the upper crust. For instance, the Moho profiles of ENH and CD2 are characterized by multiple peaks ahead of the peak with maximum amplitude (Figure 8c), which indicates a strong velocity gradient above the Moho discontinuity. In the recent receiver function studies of 11 IRIS GSN stations in China by Huang *et al.* [2008], the crustal thickness beneath ENH was found to be 40 km, about 6 km thinner than our result. The  $V_p/V_s$  ratio determined by their data set is 1.89, considerably larger than our result at about 1.75. This  $H - \kappa$  pair is close to the other peak displayed on our  $s(H, \kappa)$  contour map (Figure 4) with  $H = 35.9$  km and  $\kappa = 1.996$ . However,

we did not choose this peak because of the abnormally high  $V_p/V_s$  ratio. Both Huang *et al.* [2008] and our data showed complicated receiver functions, which is a manifestation of local heterogeneity within the crust beneath ENH. It is very likely that the complicated multiples caused a strong trade-off between  $H$  and  $\kappa$ , which led to the apparent discrepancy between Huang *et al.* [2008] and our measurements.

[35] We could not measure the crustal thickness and  $V_p/V_s$  ratio simultaneously at station CD2 because we could not reconcile the discrepancies of all receiver functions, which likely reflect a high level of lateral heterogeneity in the crust around this station. Wang *et al.* [2007] deployed two crossed DSS profiles through the eastern margin of the Tibetan Plateau (P2 in Figure 8a). The E-W trending line AA' started at the Songpan-Ganzi terrane and ended at the Sichuan basin, while the NNE trending line BB' crossed the Songpan-Ganzi terrane. The average crustal thickness along the profiles is found to be 62 km and 43 km beneath the Songpan-Ganzi terrane and the Sichuan basin, respectively. CD2 is located at the boundary of the Songpan-Ganzi terrane and the Sichuan basin, approximately the middle point between the northern end of line BB' and the eastern end of line AA' (Figure 8a). We made use of the teleseismic events from the southwest and northwest direction (BAZ about  $165^\circ - 360^\circ$ ) to obtain a crustal thickness of about 52 km, which is within the range of results from those two profile sources. Lou *et al.* [2008] analyzed seismic waveform data on 20 broadband stations near the Longmen mountains to investigate the deep structure around the source of the 12 May 2008 Wenchuan earthquake. Their receiver function analysis indicated the crustal thickness and  $V_p/V_s$  ratio beneath CD2 are about 42.5 km and 1.80, respectively. When we used the same procedure as applied on CN2 to examine the back-azimuthal dependence of the crustal structure at CD2 (Figure 12b), we found that the results of Lou *et al.* [2008] are consistent with ours at back-azimuthal range from  $80^\circ$  to  $140^\circ$ .

[36] Wang *et al.* [2000] studied a seismic refraction profile which started from the Hefei basin of the Sino-Korean craton and extended to the Yangtze craton across the Dabie Shan orogenic belt with a N25°E trend (P1 in Figure 8a). Stations HEF and NNC are located at the northern and southern end of the profile, respectively, and NJ2 and WHN are about 150 km away from the profile. These four stations are on the cratonic blocks with HEF and NJ2 being in the northern side and WHN and NNC in the southern side of the Dabie mountain, the orogenic belt that separates the Sino-Korean and Yangtze craton. Crustal thickness beneath these four stations is quite uniform, between 30.7 and 33.5 km, which is a few kilometers thinner than the active source estimates for the two cratonic blocks (about 35 km). The crustal  $V_p/V_s$  ratios beneath HEF, NJ2, and WHN are between 1.718 ( $\sigma = 0.244$ ) and 1.734 ( $\sigma = 0.251$ ), approximately at the low bound of those measured along the profile. On the basis of Wang *et al.* [2000],  $V_p/V_s$  ratio increases from 1.71 in the upper crust to 1.78 in the lower crust. The low  $V_p/V_s$  ratios imply that the crust beneath these two cratons is dominantly felsic in composition.

[37] Zhang *et al.* [2005] analyzed the wide-angle reflected seismic data collected in a profile deployed in southeastern China extending in the NW-SE direction (P3 in Figure 8a). Station WZH located at the southeastern end of this profile

showed a crustal thickness of 29.8 km and a  $V_p/V_s$  ratio of 1.878 ( $\sigma = 0.302$ ). The estimated thickness here is compatible with the 31–32 km Moho depth identified by the profile data. Our  $V_p/V_s$  ratio is, however, considerably higher than the bulk crust average of 1.74 given by the profile data although the profile data also found that the  $V_p/V_s$  ratio of the lower crust was relatively high, between 1.75 and 1.85. We noted that the primary  $P$ -to- $S$  converted phase is relatively weak on the receiver functions of WZH compared to the crustal multiple phases, which may be associated with Moho topography that causes defocusing and focusing for different raypaths.

[38] Kan *et al.* [1986] studied the crustal structure beneath an  $H$ -shaped seismic refraction profile ( $P4$  in Figure 8a) in Yunnan province, an area in southwestern China that was significantly influenced by the active tectonics near the southeastern end of the Himalaya-Burma arc. They found a relatively low mean crustal velocity in this area, and the crustal thickness variation from 38 to 46 km. Two CNDSN stations in this province, KMI and TNC are very close to the profiles (we set TNC into the Tibetan Plateau, however). The receiver function determined crustal thickness beneath KMI at 44.1 km, a few kilometers thicker than the value at the nearest point on the profile (about 41 km). The  $V_p/V_s$  ratio beneath KMI is as low as 1.705 ( $\sigma = 0.238$ ). Our results support the conclusion derived from the low crustal velocity in the work of Kan *et al.* [1986]. The low velocity and  $V_p/V_s$  ratio all point to a crustal composition that consists mainly of metasedimentary and silicic intrusive rocks, with little mafic or ultramafic component.

#### 4.4. Northwest China

[39] This tectonic region includes two stable cratons, the Tarim basin and the Junggar basin, separated by active fold systems, the Tian Shan and the Qilian Shan. After its formation in the Carboniferous, the Tian Shan was reactivated during the late Mesozoic and the late Cenozoic as a result of a series of collisional events, such as the Qiangtang-Tarim and the Qiangtang-Lhasa collisions that occurred far to the south of the range [Vermeesch, 2003]. These collisional processes have made the modern Tian Shan the most spectacular intracontinental mountain range in the world, with a high topography up to 7400 m while being more than 1000 km away from the nearest plate boundary. All of the seven stations located in this region are deployed along fold systems (Figure 9a), i.e., stations LZH, GTA, and AXX are spread along the Qilian Shan, WUS, KSH, and WMQ are located along the Tian Shan system, while HTA is located at the southern boundary of the Tarim basin. Compared to the eastern part of China, Northwest China has a thick crust with a mean value of about 51.0 km (Figure 9c). Moho depth beneath KSH even reaches 60.0 km. The average crustal  $V_p/V_s$  ratio beneath this region is 1.770 ( $\sigma = 0.265$ ) (Figure 9d), considerably higher than that of eastern China. Since all seven stations are located outside of the stable cratons in this region, the measured crustal thickness and  $V_p/V_s$  ratios probably do not reflect the crustal structure of the Tarim and Junggar craton.

[40] Station AXX is located only tens of kilometers east of a refraction profile that extends southward from the southern margin of the Altai Mountains to the Qaidam basin ( $P5$  in Figure 9a). Wang *et al.* [2003] obtained a uniform

crustal thickness of 50 km across this profile. The southern half of the profile showed a low Poisson's ratio of 0.25, while the northern half had a higher Poisson's ratio of 0.26–0.27. These values agree well with our measurement at the AXX station, which shows a crustal thickness of 48.8 km and a Poisson's ratio of 0.252. Liu *et al.* [2006] studied another refraction profile that starts from the northern Songpan-Ganzi terrane, extending northeastward to the Ordos basin ( $P6$  in Figure 9a). The closest CNDSN station to this profile is LZH, which is located at approximately 100 km northwest of the shotpoint 4 in the middle of this profile. Our receiver function analysis showed that LZH is underlain by a 51.8 km thick crust with an average  $V_p/V_s$  ratio of 1.740 ( $\sigma = 0.253$ ). These values agree well with the active source results. The low  $V_p/V_s$  ratio suggests that the crust beneath the NE margin of the Tibetan Plateau is dominantly felsic in composition with an intermediate composition at the base.

#### 4.5. The Tibetan Plateau

[41] Here we refer to the plateau as the vast areas in the southwestern and central China. It is well known that the collision between India and Asia starting at approximately 45 Ma has led to the uplift of the Tibetan Plateau and the formation of the Himalaya. This most recent large-scale orogenic event has attracted a wide interest from the scientific community, but details of the seismic structure and the involved dynamic processes are still unclear. The collision has influenced the shape of China far beyond the Himalaya-Tibet orogeny. It has reactivated many other tectonic zones that are located even a few thousands kilometers away from the collision front. These include the Tian Shan, the Altai, and the Kunlun fold systems, as well as the Xianshui-He and Red River fault systems. They have far more complicated crustal structure than cratons.

[42] We analyzed a total of seven stations from this region. Stations SQH and LSA are located at the western and central Lhasa terrane, respectively, NAQ is located at the Qiangtang terrane, HTG and GOM are located at the East Kunlun fold system, and CAD and TNC are at the Sanjiang fold system (Figure 10a). The crust beneath the Tibetan Plateau is very thick. Six measurements on the Tibetan Plateau (excluding TNC) showed an average crustal thickness of 70.3 km (Figure 10c). The Moho at the central part of the Tibetan Plateau that is sampled from LSA and NAQ can reach to 79.9 km and 78.3 km, respectively, after correcting for the station elevation. Furthermore, these six measurements indicate that the crust thins gradually toward the edge of the plateau. At some stations such as CAD, SQH, and LSA, multiple weak but identifiable peaks appear ahead of the peak with the maximum amplitude that we interpreted as the crust-mantle boundary. It implies that either there exists a transition zone over tens of kilometers from the crust to the mantle or a layer with strong velocity variation in the lowermost crust. The mean  $V_p/V_s$  ratio of this area is about 1.726 ( $\sigma = 0.247$ ) if TNC is excluded (Figure 10d). We found that the  $H - \kappa$  trade-off is relatively large in this region (Figure 4). This is probably related to the deep Moho that results in weak reverberations.

[43] An east-west seismic profile was conducted across the central Tibetan Plateau by the Sino-French joint seismic program ( $P7$  in Figure 10a), intersecting a line between

NAQ and LSA. *Zhang and Klemperer* [2005] studied the wide-angle reflection data of this profile and suggested that the Moho may reach down to 75–80 km along the eastern part of the profile. Their result is compatible with our measurement of 78.3 km beneath NAQ, which is located at about 100 km away from the profile. *Owens and Zandt* [1997] observed unusually high Poisson's ratio ( $\sigma > 0.30$ ) in the north of the Tibetan Plateau. Together with the presence of hot springs and high electrical conductivity [*Wei et al.*, 2001; *Unsworth et al.*, 2004], these seismological observations have been interpreted as evidence for partial melting in the lower crust beneath the northern part of the plateau. A lab experiment showed that granite with 5% partial melt has a Poisson's ratio of 0.31 as compared to 0.24 when no melt is present [*Watanabe*, 1993], whereas it is very rare for unmelted crustal rocks to have a Poisson's ratio larger than 0.30 [*Christensen*, 1996]. Such high Poisson's ratios are not observed from our samples on the Tibetan Plateau, which is probably due to the sparse station distribution. We found several peaks in the  $H - \kappa$  map of the NAQ station, which is probably caused by local anomalies beneath the station.

[44] *Zhao et al.* [2006] studied a seismic refraction/wide reflection profile across the Altyn Tagh Range and its adjacent basins (P8 in Figure 10a). Station HTG is near shotpoint 8 of this profile. The crustal thickness revealed from the active source data is about 60 km. We found two peaks in the  $s(H, \kappa)$  contour map of this station (Figure 4), and picked the one that is more consistent with their result, which is 56.0 km. The corresponding  $V_p/V_s$  ratio is 1.744 ( $\sigma = 0.255$ ) indicating an intermediate composition. There were a few 2-D seismic surveys inside the Qaidam basin using active sources [e.g., *Cui et al.*, 1995; *Vergne et al.*, 2002]. Station GOM is located near several such 2-D profiles (P9 in Figure 10a). The crustal thickness around GOM obtained from the active sources varies from 55 to 65 km, and the Poisson's ratio is about 0.256. We obtained a crustal thickness of 65.6 km and a Poisson's ratio of 0.247 at station GOM. We could not find any obvious reasons for the large discrepancy of Poisson's ratio between the active source and receiver function results.

[45] Station TNC is located at the Sanjiang fold system. The crustal structure beneath this station also exhibits considerable variations with back azimuths (Figure 12c). We chose the result from  $\text{BAZ} = 20^\circ - 60^\circ$  (39.0 km), which is more consistent with previous observations near the station (P4 in Figure 10a) [*Kan et al.*, 1986]. We did not include the  $V_p/V_s$  ratio measurement for TNC in creating Figure 5b as the Moho multiples were rather weak and complicated and could not be uniquely identified. In a recent receiver function analysis for the crust and upper mantle structure around Yunnan province, *Li et al.* [2009] determined that the crust beneath TNC has thickness about 35 km and  $V_p/V_s$  ratio about 1.87 using the similar  $H - \kappa$  domain search technique. These measurements appeared to be consistent with what are shown in the back azimuth range of  $260^\circ - 310^\circ$ . We thus believe that discrepancy arises probably from the large lateral variations around this station.

#### 4.6. Comparison to Other Studies

[46] Since 1958, more than 6000 km of refraction and wide reflection seismic profiles have been deployed in

China. *Li et al.* [2006] compiled part of the results from these surveys. We cited nine seismic refraction/wide reflection profiles that happened to go through or close to the CNDN stations. We made a superficial comparison of the crustal structure derived from the two types of seismic studies. The receiver function models for some stations, such as HEF, NJ2, WHN, AXX, and LZH, are in a good agreement with the  $P$  and/or  $S$  wave velocity structure derived from active source data. As the active source and receiver function data cover very different frequency bands, the consistency in Moho depth estimates indicates that the Moho beneath these stations must be a sharp boundary with a thickness of less than 2 km. On the other hand, we also found a number of stations whose receiver function models are considerably different from the active source results. The discrepancy could be caused by different definitions of the Moho and different sampling nature in active and passive seismic data. The active source data usually employ high-frequency seismic waves (about 5 Hz) while the dominant frequency in the teleseismic receiver function data is much lower (about 0.5 Hz). Also, active source reflection data sample the Moho from the upper side while the receiver function primary wave illuminates the boundary from the lower side. If the crust-mantle transition occurs gradually, the estimated Moho depth depends on the wavelength of the sampling waves. While high-frequency active source data more or less report the depth associated with a rapid change in velocity, the long-wavelength teleseismic waves are likely to give the average depth of the whole transition. Furthermore, reliable  $S$  wave velocity models are very difficult to obtain in these active seismic source experiments because the arrivals of undeveloped  $S$  waves from active sources are difficult to be picked from the short-period vertical seismometers that are commonly used in these experiments. The inferred  $V_p/V_s$  ratio could be severely biased with the active source data. Therefore, it is hard to compare the  $V_p/V_s$  ratio derived from the two types of data.

[47] A variety of studies have addressed the relationship between crustal thickness and the  $V_p/V_s$  ratios for a variety of crustal types, as well as their relationship with crustal age, to cast light on the formation and evolution of continental crust [e.g., *Clarke and Silver*, 1993; *Christensen and Mooney*, 1995; *Zandt and Ammon*, 1995; *Chevrot and van der Hilst*, 2000; *Niu and James*, 2002; *Nair et al.*, 2006]. Our measurements for China have considerable discrepancies from the observations on other continents, as well as on the global scale. The average Poisson's ratios of the Mesozoic-Cenozoic orogenic belts in western China are fairly consistent with the global values derived by *Zandt and Ammon* [1995]. In the eastern part of China, the low Poisson's ratios measured for the Ordos, Sino-Korean, and Yangtze craton with an Archean basement suggest a more felsic crustal composition than the global average (0.27–0.29 by *Zandt and Ammon* [1995]). In addition to this study, other results from China also appeared to be contradictory to global crustal models with a mafic/ultramafic layer in the lowermost crust [e.g., *Gao et al.*, 1998; *Li et al.*, 2006], although considerable discrepancies exist in these studies. On the other hand, we have to be cautious in comparing the global estimates due to the fact that most global studies on crustal velocity and composition have been biased toward North America, Western Europe, and Australia [*Holbrook et al.*, 1992;

Christensen and Mooney, 1995; Zandt and Ammon, 1995] and these global models may not reflect the crustal structure and composition beneath China.

## 5. Conclusions

[48] We introduced a modification to the conventional “ $H - \kappa$ ” method to reduce the trade-off between crustal thickness and  $V_p/V_s$  ratio, and applied the technique to a large set of high-quality broadband data recorded at 48 CNDSN stations to measure crustal thickness and  $V_p/V_s$  ratio beneath the stations. Our receiver function analysis revealed the following features of the crust and the Moho boundary beneath China:

[49] 1. The Moho beneath the eastern portion of China is relatively shallow, flat, and sharp. The thinnest crust lies along the coast of the south China fold system and the eastern part of the Yangtze craton. The crust gradually thickens by a few kilometers toward the northeast in the NNE direction. In western China, the Moho depth varies from 46 to 84 km and shows a good correlation with surface topography. The largest topographic relief of the Moho discontinuity occurs at the edge of the Tibetan Plateau, whereas the thickest crust, which may extend as much as 84 km, is located at the central part of the plateau.

[50] 2. The transition between the two distinct crustal regions occurs within a narrow NS trending belt between 100°E and 110°E, the so-called N-S belt. The belt is also featured by high seismicity and a distinct gravity anomaly.

[51] 3. The low  $V_p/V_s$  ratios of the Precambrian cratons in eastern China render the mean over the whole Chinese crust to about 1.730 ( $\sigma = 0.249$ ), remarkably lower than the global average 1.78 ( $\sigma = 0.27$ ) for the continental crust. On average, the Yangtze craton has a lower  $V_p/V_s$  ratio than the Ordos and the Sino-Korea craton. The low  $V_p/V_s$  observed here suggests a general absence of a mafic layer in the lowermost crust beneath China, and we speculate that a large-scale delamination event may be responsible for the removal of this mafic layer. The  $V_p/V_s$  ratio (Poisson’s ratio) measured in the western part of China is 1.732–1.770 ( $\sigma = 0.250$ – $0.265$ ), roughly consistent with the global estimates of the Mesozoic-Cenozoic orogenic belts [Zandt and Ammon, 1995].

[52] 4. Neither crustal thickness nor  $V_p/V_s$  ratio appears to have an obvious dependence on crustal age.

[53] **Acknowledgments.** The authors thank Y. Sun and N. Toksöz from MIT for providing the crustal and upper mantle velocity model for China from their tomographic studies. The authors are greatly indebted to Walter Mooney from USGS for providing the information of important DSS profiles deployed in China, and insightful suggestions and comments. The authors also thank the Associate Editor and two anonymous reviewers for their constructive reviews that improved the manuscript significantly.

## References

- Ammon, C. J. (1991), The isolation of receiver effects from teleseismic  $P$  waveforms, *Bull. Seismol. Soc. Am.*, *81*, 2504–2510.
- Ammon, C. J., and G. Zandt (1993), The receiver structure beneath the southern Mojave Block, California, *Bull. Seismol. Soc. Am.*, *83*, 737–755.
- Beckers, J., S. Y. Schwartz, and T. Lay (1994), The velocity structure of the crust and upper mantle under China from broadband  $P$  and  $PP$  waveform analysis, *Geophys. J. Int.*, *119*, 574–594, doi:10.1111/j.1365-246X.1994.tb00143.x.
- Bump, H. A., and A. F. Sheehan (1998), Crustal thickness variations across the northern Tien Shan from teleseismic receiver functions, *Geophys. Res. Lett.*, *25*, 1055–1058, doi:10.1029/98GL00516.
- Chevrot, S., and R. D. van der Hilst (2000), The Poisson ratio of the Australian crust: Geological and geophysical implications, *Earth Planet. Sci. Lett.*, *183*, 121–132, doi:10.1016/S0012-821X(00)00264-8.
- Christensen, N. I. (1996), Poisson’s ratio and crustal seismology, *J. Geophys. Res.*, *101*, 3139–3156, doi:10.1029/95JB03446.
- Christensen, N. I., and W. D. Mooney (1995), Seismic velocity structure and composition of the continental crust: A global view, *J. Geophys. Res.*, *100*, 9761–9788, doi:10.1029/95JB00259.
- Clarke, T. J., and P. G. Silver (1993), Estimation of crustal Poisson’s ratio from broad band teleseismic data, *Geophys. Res. Lett.*, *20*, 241–244, doi:10.1029/92GL02922.
- Clitheroe, G., O. Gudmundsson, and B. L. N. Kennett (2000), Sedimentary and upper crustal structure of Australia from receiver functions, *Aust. J. Earth Sci.*, *47*(2), 209–216, doi:10.1046/j.1440-0952.2000.00774.x.
- Cui, Z., Q. Li, C. Wu, Z. Yin, and H. Liu (1995), The crustal and deep structures in Golmud-Ejin Qi GGT, *Acta Geophys. Sin.*, *38*, 15–28.
- Davis, G. A., Y. Zheng, C. Wang, B. J. Darby, C. Zhang, and G. Gehrels (2001), Mesozoic tectonic evolution of the Yanshan fold and thrust belt, with emphasis on Hebei and Liaoning provinces, northern China, *Geol. Soc. Am. Mem.*, *194*, 171–197.
- Durrheim, R. J., and W. D. Mooney (1994), Evolution of the Precambrian lithosphere: Seismological and geochemical constraints, *J. Geophys. Res.*, *99*, 15,359–15,374, doi:10.1029/94JB00138.
- Efron, B., and R. Tibshirani (1986), Bootstrap methods for standard errors, confidence intervals, and other measures of statistical accuracy, *Stat. Sci.*, *1*, 54–75, doi:10.1214/ss/1177013815.
- Feng, R., J. Zhu, and Y. Ding (1981), A study on the crustal structure of China with surface waves (in Chinese), *Acta Seismol. Sin.*, *3*(4), 335–350.
- Gadallah, M., and R. L. Fisher (2005), *Applied Seismology: A Comprehensive Guide to Seismic Theory and Application*, chap. 6, pp. 147–287, PennWell Books, Tulsa, Okla.
- Gao, S., B. R. Zhang, Z. M. Jin, H. Kern, T. C. Luo, and Z. D. Zhao (1998), How mafic is the lower continental crust?, *Earth Planet. Sci. Lett.*, *161*, 101–117, doi:10.1016/S0012-821X(98)00140-X.
- Graham, S. A., M. S. Hendrix, C. L. Johnson, D. Badamgarav, G. Badarch, J. Amory, M. Porter, R. Barshold, L. E. Webb, and B. R. Hacker (2001), Sedimentary record and tectonic implications of Mesozoic rifting in Southeast Mongolia, *Geol. Soc. Am. Bull.*, *113*, 1560–1579, doi:10.1130/0016-7606(2001)113<1560:SRATIO>2.0.CO;2.
- Holbrook, W. S., W. D. Mooney, and N. I. Christensen (1992), The seismic velocity structure of the deep continental crust, in *Continental Lower Crust*, edited by D. M. Fountain, R. Arculus, and R. Kay, pp. 21–43, Elsevier, New York.
- Huang, J.-P., J.-J. Chong, and S.-D. Ni (2008), Inverting the crustal thickness under the stations of China via H-Kappa method (in Chinese), *J. Univ. Sci. and Technol. China*, *38*, 33–40.
- Huang, T. K., C. Jen, C. Jiang, Z. Chang, and D. Chin (1980), *The Geotectonic Evolution of China*, 124 pp., Academic, Beijing.
- Kan, R., H. Hu, R. Zeng, W. D. Mooney, and T. V. McEvilly (1986), Crustal structure of Yunnan Province, People’s Republic of China, from seismic refraction profiles, *Science*, *234*, 433–437, doi:10.1126/science.234.4775.433.
- Kind, R., et al. (2002), Seismic images of crust and upper mantle beneath Tibet: Evidence for Eurasian plate subduction, *Science*, *298*, 1219–1221.
- Langston, C. A. (1979), Structure under Mount Rainier, Washington, inferred from teleseismic body waves, *J. Geophys. Res.*, *84*, 4749–4762, doi:10.1029/JB084iB09p04749.
- Langston, C. A. (1994), An integrated study of crustal structure and regional wave propagation for southeastern Missouri, *Bull. Seismol. Soc. Am.*, *84*, 105–118.
- Li, S. L., and W. D. Mooney (1998), Crustal structure of China from deep seismic sounding profiles, *Tectonophysics*, *288*, 105–113, doi:10.1016/S0040-1951(97)00287-4.
- Li, S. L., W. D. Mooney, and J. Fan (2006), Crustal structures of mainland China from deep seismic sounding data, *Tectonophysics*, *420*, 239–252, doi:10.1016/j.tecto.2006.01.026.
- Li, Y.-H., Q.-J. Wu, X.-B. Tian, R.-Q. Zhang, J.-T. Pan, and R.-S. Zeng (2009), Crustal structure in the Yunnan region determined by modeling receiver functions (in Chinese), *Chin. J. Geophys.*, *52*(1), 67–80.
- Li, Z. X., X. H. Li, P. D. Kinny, and J. Wang (1999), The breakup of Rodinia: Did it start with a mantle plume beneath South China?, *Earth Planet. Sci. Lett.*, *173*, 171–181, doi:10.1016/S0012-821X(99)00240-X.
- Liang, C., X. Song, and J. Huang (2004), Tomographic inversion of  $Pn$  travel times in China, *J. Geophys. Res.*, *109*, B11304, doi:10.1029/2003JB002789.
- Ligorria, J. P., and C. J. Ammon (1999), Iterative deconvolution and receiver-function estimation, *Bull. Seismol. Soc. Am.*, *89*, 1395–1400.
- Liu, M., W. D. Mooney, S. Li, N. Okaya, and S. Detweiler (2006), Crustal structure of the northeastern margin of the Tibetan Plateau from the

- Songpan-Ganzi terrane in the Ordos basin, *Tectonophysics*, 420, 253–266, doi:10.1016/j.tecto.2006.01.025.
- Lou, H., C.-Y. Wang, Z.-Y. Lu, Z.-X. Yao, R.-G. Dai, and H.-C. You (2008), The deep tectonic environment of 2008, Ms 8.0, Wenchuan earthquake: The joint explanation of teleseismic *P* wave receiver function and Bouguer anomalies in gravity (in Chinese), *Sci. China D*, 38(10), 1207–1220.
- Ma, Y., and H. Zhou (2007), Crustal thickness and Poisson's ratios in China by joint analysis of teleseismic receiver function and Rayleigh wave dispersion, *Geophys. Res. Lett.*, 34, L12304, doi:10.1029/2007GL029848.
- Mahdi, H., and G. L. Pavlis (1998), Velocity variations in the crust and upper mantle beneath the Tien Shan inferred from Rayleigh wave dispersion: Implications for tectonic and dynamic processes, *J. Geophys. Res.*, 103, 2693–2703.
- Mangino, S., K. Priestley, and J. Ebel (1999), The receiver structure beneath the China digital seismograph network stations, *Bull. Seismol. Soc. Am.*, 89, 1053–1076.
- Mitra, S., K. Priestley, A. K. Bhattacharyya, and V. K. Gaur (2005), Crustal structure and earthquake focal depths beneath northeastern India and southern Tibet, *Geophys. J. Int.*, 160, 227–248, doi:10.1111/j.1365-246X.2004.02470.x.
- Mooney, W. D., G. Laske, and T. G. Masters (1998), CRUST 5.1: A global crust model at  $5^\circ \times 5^\circ$ , *J. Geophys. Res.*, 103, 727–747, doi:10.1029/97JB02122.
- Nair, S. K., S. S. Gao, K. H. Liu, and P. G. Silver (2006), Southern African crustal evolution and composition: Constraints from receiver function studies, *J. Geophys. Res.*, 111, B02304, doi:10.1029/2005JB003802.
- Nguuri, T. K., J. Gore, D. E. James, S. J. Webb, C. Wright, T. G. Zengeni, O. Gwawava, J. A. Snoke, and the Kaapvaal Seismic Group (2001), Crustal structure beneath southern Africa and its implications for the formation and evolution of the Kaapvaal and Zimbabwe cratons, *Geophys. Res. Lett.*, 28, 2501–2504, doi:10.1029/2000GL012587.
- Niu, F., and D. E. James (2002), Fine structure of the lowermost crust beneath the Kaapvaal craton and its implications for crustal formation and evolution, *Earth Planet. Sci. Lett.*, 200, 121–130, doi:10.1016/S0012-821X(02)00584-8.
- Niu, F., and H. Kawakatsu (1996), Complex structure of the mantle discontinuities at the tip of the subducting slab beneath the northeast China: A preliminary investigation of broadband receiver functions, *J. Phys. Earth*, 44, 701–711.
- Niu, F., T. Bravo, G. Pavlis, F. Vernon, H. Rendon, M. Bezada, and A. Levander (2007), Receiver function study of the crustal structure of the southeastern Caribbean plate boundary and Venezuela, *J. Geophys. Res.*, 112, B11308, doi:10.1029/2006JB004802.
- Owens, T. J., and G. Zandt (1997), Implications of crustal property variations for models of Tibetan Plateau evolution, *Nature*, 387, 37–43, doi:10.1038/387037a0.
- Owens, T. J., G. Zandt, and S. R. Taylor (1984), Seismic evidence for an ancient rift beneath the Cumberland Plateau, Tennessee: A detailed analysis of broadband teleseismic *P* waveforms, *J. Geophys. Res.*, 89, 7783–7795, doi:10.1029/JB089iB09p07783.
- Owens, T. J., S. R. Taylor, and G. Zandt (1987), Crustal structure at regional seismic test network stations determined from inversion of broadband teleseismic *P* waveforms, *Bull. Seismol. Soc. Am.*, 77, 631–632.
- Pei, S., Z. Xu, and S. Wang (2004), Sn wave tomography of the uppermost mantle beneath the China continent and adjacent regions, *Chin. J. Geophys.*, 47, 278–284.
- Pei, S., J. Zhao, Y. Sun, Z. Xu, S. Wang, H. Liu, C. A. Rowe, M. N. Toksöz, and X. Gao (2007), Upper mantle seismic velocities and anisotropy in China determined through *Pn* and *Sn* tomography, *J. Geophys. Res.*, 112, B05312, doi:10.1029/2006JB004409.
- Reading, A., B. Kennett, and M. Sambridge (2003), Improved inversion for seismic structure using transformed, *S*-wavevector receiver functions: Removing the effect of the free surface, *Geophys. Res. Lett.*, 30(19), 1981, doi:10.1029/2003GL018090.
- Rudnick, R. L. (1995), Making continental crust, *Nature*, 378, 571–578, doi:10.1038/378571a0.
- Sherrington, H. F., G. Zandt, and A. Frederiksen (2004), Crustal fabric in the Tibetan Plateau based on waveform inversions for seismic anisotropy parameters, *J. Geophys. Res.*, 109, B02312, doi:10.1029/2002JB002345.
- Sun, Y., and M. N. Toksöz (2006), Crustal structure of China and surrounding regions from *P* wave traveltimes tomography, *J. Geophys. Res.*, 111, B03310, doi:10.1029/2005JB003962.
- Sun, Y. S., X. Li, S. Kuleli, F. D. Morgan, and M. N. Toksöz (2004), Adaptive moving window method for 3-D *P*-velocity tomography and its application in China, *Bull. Seismol. Soc. Am.*, 94, 740–746, doi:10.1785/0120030129.
- Svenningsen, L., and B. H. Jacobsen (2004), Comment on “Improved inversion for seismic structure using transformed, *S*-wavevector receiver functions: Removing the effect of the free surface” by Anya Reading, Brain Kennett, and Malcolm Sambridge, *Geophys. Res. Lett.*, 31, L24609, doi:10.1029/2004GL021413.
- Tarkov, A. P., and V. V. Vavakin (1982), Poisson's ratio behavior in crystalline rocks: Application to the study of the Earth's interior, *Phys. Earth Planet. Inter.*, 29, 24–29, doi:10.1016/0031-9201(82)90134-0.
- Tkalčić, H., M. Pasyanos, A. Rodgers, R. Gök, W. Walter, and A. Al-Amri (2006), A multi-step approach in joint modelling of surface wave dispersion and teleseismic receiver functions: Implications for lithospheric structure of the Arabian peninsula, *J. Geophys. Res.*, 111, B11311, doi:10.1029/2005JB004130.
- Unsworth, M., W. Wei, A. G. Jones, S. Li, P. Bedrosian, J. Booker, S. Jin, M. Deng, and H. Tan (2004), Crustal and upper mantle structure of northern Tibet imaged with magnetotelluric data, *J. Geophys. Res.*, 109, B02403, doi:10.1029/2002JB002305.
- Vergne, J., G. Wittlinger, Q. Hui, P. Tapponnier, G. Poupinet, J. Mei, G. Herquel, and A. Paul (2002), Seismic evidence for stepwise thickening of the crust across the NE Tibetan Plateau, *Earth Planet. Sci. Lett.*, 203, 25–53, doi:10.1016/S0012-821X(02)00853-1.
- Vermeesch, P. (2003), A second look at the geologic map of China: The “Stoss approach”, *Int. Geol. Rev.*, 45, 119–132, doi:10.2747/0020-6814.45.2.119.
- Vinnik, L. P. (1977), Detection of waves converted from *P* to *SV* in the mantle, *Phys. Earth Planet. Inter.*, 15, 39–45, doi:10.1016/0031-9201(77)90008-5.
- Wang, C.-Y., R.-S. Zeng, W. D. Mooney, and B. R. Hacker (2000), A crustal model of the ultrahigh-pressure Dabie Shan orogenic belt, China, derived from deep seismic refraction profiling, *J. Geophys. Res.*, 105, 10,857–10,869, doi:10.1029/1999JB900415.
- Wang, C.-Y., W.-B. Han, J.-P. Wu, H. Lou, and W. W. Chan (2007), Crustal structure beneath the eastern margin of the Tibetan Plateau and its tectonic implications, *J. Geophys. Res.*, 112, B07307, doi:10.1029/2005JB003873.
- Wang, Y., W. D. Mooney, X. Yuan, and R. G. Coleman (2003), The crustal structure from the Altai Mountains to the Altyn Tagh fault, northwest China, *J. Geophys. Res.*, 108(B6), 2322, doi:10.1029/2001JB000552.
- Wang, Y., G. A. Houseman, G. Lin, F. Guo, Y.-J. Wang, W.-M. Fan, and X. Chang (2005), Mesozoic lithospheric deformation in the North China block: Numerical simulation of evolution from orogenic belt to extensional basin system, *Tectonophysics*, 405, 47–63, doi:10.1016/j.tecto.2005.05.012.
- Watanabe, T. (1993), Effects of water and melt on seismic velocities and their application to characterization of seismic reflectors, *Geophys. Res. Lett.*, 20, 933–2936, doi:10.1029/93GL03170.
- Wei, W., et al. (2001), Detection of widespread fluids in the Tibetan crust by magnetotelluric studies, *Science*, 292, 716–718, doi:10.1126/science.1010580.
- Wittlinger, G., J. Vergne, P. Tapponnier, V. Farra, G. Poupinet, M. Jiang, H. Su, G. Herquel, and A. Paul (2004), Teleseismic imaging of subducting lithosphere and Moho offsets beneath western Tibet, *Earth Planet. Sci. Lett.*, 221, 117–130, doi:10.1016/S0012-821X(03)00723-4.
- Wolfe, C. J., and F. L. Vernon (1998), Shear-wave splitting at central Tien Shan: Evidence for rapid variation of anisotropic patterns, *Geophys. Res. Lett.*, 25, 1217–1220.
- Yin, A., and T. M. Harrison (2000), Geologic evolution of the Himalayan-Tibetan orogen, *Annu. Rev. Earth Planet. Sci.*, 28, 211–280, doi:10.1146/annurev.earth.28.1.211.
- Yin, A., and S. Y. Nie (1996), A Phanerozoic palinspastic reconstruction of China and its neighboring regions, in *The Tectonic Evolution of Asia*, edited by A. Yin and T. M. Harrison, pp. 442–485, Cambridge Univ. Press, New York.
- Yuan, X., S. Wang, L. Li, and J. Zhu (1986), A geophysical investigation of the deep structure in China, in *Reflection Seismology: A Global Perspective*, *Geodyn. Ser.*, vol. 13, pp. 151–160, AGU, Washington, D. C.
- Zandt, G., and C. J. Ammon (1995), Continental crust composition constrained by measurements of crustal Poisson's ratio, *Nature*, 374, 152–154, doi:10.1038/374152a0.
- Zandt, G., S. C. Myers, and T. C. Wallace (1995), Crust and mantle structure across the basin and range: Colorado plateau boundary at 37N latitude and implications for Cenozoic extensional mechanism, *J. Geophys. Res.*, 100, 10,529–10,548, doi:10.1029/94JB03063.
- Zhang, Z., and S. L. Klemperer (2005), West-east variation in crustal thickness in northern Lhasa block, central Tibet, from deep seismic sounding data, *J. Geophys. Res.*, 110, B09403, doi:10.1029/2004JB003139.
- Zhang, Z., J. Badal, Y. Li, Y. Chen, L. Yang, and J. Teng (2005), Crust-upper mantle seismic velocity structure across southeastern China, *Tectonophysics*, 395, 137–157, doi:10.1016/j.tecto.2004.08.008.
- Zhao, J., W. D. Mooney, X. Zhang, Z. Li, Z. Jin, and N. Okaya (2006), Crustal structure across the Altyn Tagh Range at the northern margin of the Tibetan Plateau and tectonic implications, *Earth Planet. Sci. Lett.*, 241, 804–814, doi:10.1016/j.epsl.2005.11.003.

Zhou, M. F., D. P. Yan, A. K. Kennedy, Y. Li, and J. Ding (2002), SHRIMP U-Pb zircon geochronological and geochemical evidence for neoproterozoic arc-magmatism along the western margin of the Yangtze block, South China, *Earth Planet. Sci. Lett.*, *196*, 51–67, doi:10.1016/S0012-821X(01)00595-7.

Zhu, L., and H. Kanamori (2000), Moho depth variation in southern California from teleseismic receiver functions, *J. Geophys. Res.*, *105*, 2969–2980.

F. Niu, Department of Earth Science, Rice University, 6100 Main St., MS 126, PO Box 1892, Houston, TX 77005, USA.

Z. Huang, R. Liu, and L. Sun, Chinese Earthquake Network Center, China Earthquake Administration, PO Box 166, Beijing 100036, China.

H. Tkalčić, Research School of Earth Sciences, Australian National University, Canberra, ACT 0200, Australia.

---

W. Chan and Y. Chen, Array Information Technology, 7474 Greenway Center Dr., Ste. 600, Greenbelt, MD 20770-3504, USA. (youlin.chen@arrayinfotech.com)